International Journal of Heat and Mass Transfer 183 (2022) 122120

Contents lists available at ScienceDirect

International Journal of Heat and Mass Transfer

journal homepage: www.elsevier.com/locate/hmt

Long-term Thermo-hydraulic Response of the Shallow Subsurface soil in the Vicinity of a Buried Horizontal Heat Source

Mohammadreza Mir Tamizdoust[a], Omid Ghasemi-Fare[b,*]

[a] Ph.D. candidate, Department of Civil and Environmental Engineering, University of Louisville, USA
[b] Associate Professor, Department of Civil and Environmental Engineering, University of Louisville, USA

ARTICLE INFO

Article history:
Received 13 July 2021
Revised 5 October 2021
Accepted 16 October 2021

Keywords:
Non-isothermal multiphase flow
Non-equilibrium phase change
Film flow
Buried heat source

ABSTRACT

Heat and mass transfer in the shallow subsurface and in the vicinity of buried heat sources has been often studied based on rather simplifying assumptions, such as the Equilibrium Phase Change (EPC), disregarding film flow, and adsorptive soil-water characteristics. In this study, a fully coupled non-isothermal multiphase flow model is developed that utilizes the Non-equilibrium Phase Change (NEPC) approach. First, the performance of the EPC and NEPC approaches is assessed and validated against the in-field experimental data. The second and main objective of this study is to analyze the thermo-hydraulic response of granular soil close to a buried horizontal heat source (e.g., electrical cables) for one year under real meteorological conditions. Numerical results indicate that the NEPC model has higher robustness in predicting the volumetric water content in the soil close to the soil-atmospheric boundary. However, NEPC and EPC approaches estimate the same temperature variations in the soil. In the case of precipitation (e.g., rainfall), the NEPC model predicts higher degrees of saturation in deeper soil in which the infiltrated water reaches 150 cm below the surface, while, in the EPC model, the infiltrated water barely reaches the 100 cm depth. The increase in moisture content close to the heat source facilitates the heat transfer in the medium and thus results in a 40% to 50% reduction in soil temperature close to the heat source. An accurate prediction of the soil moisture content in the medium is needed to evaluate the performance and thermal capacity of buried electrical cables. Furthermore, the heating/cooling cycles contribute to gradually drying the soil in the vicinity of the heater until the hydraulically equilibrated condition is attained.

1. Introduction

The evaluation of heat and mass transfer close to the soil-atmosphere boundary has been the subject of many numerical and experimental studies over the past years in the geotechnical and geoenvironmental engineering designs [1–5]. In the shallow subsurface, evaporation and precipitation are the most important factors in water resources management as they directly affect the thermal fluctuations and moisture migration through soils [6]. Therefore, many numerical simulations have been conducted to assess non-isothermal hydrological cycles in global and local scales [7]. The evaporation rate is governed by the atmospheric demand or the soil's hydraulic state depending on the water availability close to the evaporative boundary [8]. The evaporation rate is traditionally calculated from the balance of thermal energy and fluid mass at the soil-atmosphere boundary. When enough liquid water is supplied to this boundary, the evaporation process is fast and intense, and depends mostly on the atmospheric condition. After the desaturation of the top layer of the soil and the disruption of the liquid conductivity from the drying front to the soil surface, the moisture transfers through vapor diffusion which drastically reduces the evaporation rate [9]. In the field conditions, precipitation plays a major role in the evaporation process as it can recharge the water storage in the top layer of soils. Furthermore, water infiltration into the soil, ponding, and runoff affect the evaporation from the soil surface, ground water recharge, and mechanical slope stability [10,11].

Many advancements have been achieved in recent years to quantify the evaporation process from the soil's surface to understand the interaction of energy and mass balances at the soil-atmospheric boundary and the internal heat and mass transfer through the soil [12–15]. Additionally, many numerical studies have been conducted based on the assumption of Equilibrium Phase Change (EPC) which are inspired by the pioneer work of Philip and De Vries [16]. However, this assumption has been relaxed by using the Non-equilibrium Phase Change (NEPC) approach

* Corresponding author.
E-mail addresses: m.mirtamizdoust@louisville.edu (M.M. Tamizdoust), omid.ghasemifare@louisville.edu (O. Ghasemi-Fare).

https://doi.org/10.1016/j.ijheatmasstransfer.2021.122120
0017-9310/

in recent years based on experimental observations [17–20]. The NEPC approach has shown promising results when utilized to simulate laboratory-scale experiments [21,22], extreme heating due to wildfires [23,24], and the evaporation from bare-soils [19,25-27].

Moreover, soil hydraulic properties such as the Soil-water Retention Characteristics (SWRC) and the Hydraulic Conductivity Function (HCF), and soils' thermal properties such as the Thermal Conductivity Function (TCF) are key features in the numerical modeling to couple heat, liquid, and vapor flow as they are nonlinearly depend on the temperature and the degree of saturation [20,28,29]. In particular, past studies have discussed the fact that the hydraulic behavior of soils in the wet condition (high and intermediate liquid saturation) is affected by capillary force, while in the dry condition, it is dominated by adsorptive forces where the liquid transport is controlled by film flow [30,31]. Therefore, classical SWRC and HCF models such as van Genuchten (VG) [32] and van Genuchten-Mualem (VGM) [33] have been extended to capture the full range of saturation. Recently, these extended models have been successfully implemented in a few numerical frameworks [26].

The utilization of heat exchanger geothermal piles, the soil-borehole thermal energy storage (SBTES), and buried electrical cables have been growing in the past years [34–38]. To understand the performance of the aforementioned energy geo-structures, the thermo-hydraulic (TH) and thermo-hydro-mechanical (THM) responses of the surrounding soils must be carefully evaluated [39–42]. Therefore, much effort has been devoted to simulating the heat and mass exchange across the soil-atmospheric boundary. However, most research on the coupled non-isothermal multiphase flow in the presence of buried horizontal or vertical heat sources in the vadose zone are based on simplified assumptions [43–46]. The unsaturated thermal conductivity of soils directly influences the heat dissipation from the heat source in the soil media. The decrease in water content lowers the thermal conductivity of the medium and thus, the temperature cannot propagate easily through the soil and accumulates in the vicinity of the heater which leads to locally intense drying of the soil. This phenomenon is not favorable for buried high voltage electrical cables as it may defect the insulation around the cable [47], nor for horizontal and vertical heat exchanger tubes as it may reduce the energy efficiency of the geothermal heat exchangers such as passive geothermal energy systems that transfer heat from the buildings to the ground [48–51]. The critical temperature that electrical cables can withstand has been the subject of many studies; however, most of them considered simplifying assumptions and performed decoupled TH models in their thermal simulations [47]. In addition, since electrical cables are buried in the shallow subsurface, meteorological conditions (evaporation and precipitation) can drastically affect the thermal and hydraulic conditions of the soils surrounding these cables. However, to the authors' knowledge, only a few studies have considered the effect of the soil-atmospheric boundary on the thermo-hydraulic responses of the soils surrounding embedded heat sources under the real meteorological condition [43].

In this study, the long-term (one year) non-isothermal multiphase flow is analyzed in the vicinity of a buried heat source (e.g., electrical high voltage cable) in unsaturated soil by utilizing the NEPC model while considering the water infiltration from either rainfall or irrigation. In the next section, major components of the thermo-hydraulic model are presented. Then, the numerical model is validated against the temperature and the volumetric moisture content measured in a field- condition. The difference in NEPC and EPC approaches are also discussed by comparing the numerical results with experimental observations. Next, the validated model is used to simulate heat and moisture transport around a shallow horizontal heat source subjected to heating and heating/cooling thermal loadings while the soil is subjected to both the evaporation and the precipitation from the soil-atmospheric boundary. The present research aims to answer the following questions:

1- What is the difference between EPC and NEPC approaches in thermo-hydraulic processes in natural in-field soils when subjected to the environmental evaporative demand and precipitation?
2- What are the advantages of the NEPC approach in evaluating the moisture and temperature distributions close to a buried horizontal heat source?
3- What is the impact of soil-atmospheric boundary condition on heat and mass transfer induced by the buried horizontal heat source in shallow subsurface?

2. The Description of Theoretical Model

Here, the non-isothermal multiphase flow is composed of the liquid (water) advection, gas (vapor and dried air) diffusion, and heat flow in convection and diffusion forms at the macroscale. The phase change is assumed to only occur between liquid water and water vapor (i.e., evaporation/condensation). Furthermore, the phase change is governed by the first-order macroscopic rate of kinetic mass transfer in porous media to consider non-equilibrium phase change. Local thermal equilibrium assumption is considered which means soil, liquid, and gas possess the same temperature in a certain location. For simplicity, the gas pressure is assumed to be constant and equal to the atmospheric pressure (=1 bar). The mathematical equations are defined in a three-dimensional Cartesian coordinate system as follows [52]:

2.1. Balance Equations

$$\text{Balance of Liquid Water}: \rho_l \frac{\partial \theta_l}{\partial p_l}\frac{\partial p_l}{\partial t} + \nabla.\mathbf{q}_l = -\dot{m} \quad (1)$$

$$\text{Balance of Water Vapor}: \frac{\partial (\theta_g \rho_v)}{\partial t} + \nabla.(-D_v \nabla \rho_v) = \dot{m} \quad (2)$$

$$\text{Balance of Energy}: (\rho C)_m \frac{\partial T}{\partial t} + \nabla.(\mathbf{q}_l C_l T - \lambda_m \nabla T) = -L_v \dot{m} \quad (3)$$

The primary variables in Equations (1), (2), and (3) are liquid pressure (p_l [Pa]), vapor density (ρ_v [kg/m^3]), and temperature (T [K]), respectively. In Equation (1), ρ_l (kg/m^3) is the density of liquid. In Equations (1) and (2), $\theta_l = nS_l$ and $\theta_g = nS_g$ (m^3/m^3) are volumetric contents of liquid and gas, respectively. Further, n (m^3/m^3) is the porosity of medium; S_l and S_g (m^3/m^3) are liquid and gas saturation degrees, respectively. ψ (Pa) is the matric suction, and is defined as: $\psi = - p_l$ by considering the force equilibrium between fluid phases. Moreover, $\partial\theta_l / \partial\psi = -\partial\theta_g / \partial\psi$ (1/Pa) is the moisture capacity and can be obtained from the SWRC constitutive relation. $\dot{m}$ (kg/m^3/s) is the rate of NEPC; positive and negative signs indicate condensation and evaporation, respectively.

In Equation (1) and (3), $\mathbf{q}_l$ (kg/m^2/s) is Darcy's liquid advective flux. In Equation (2), $D_v = =\tau\theta_g D_v{}^0$ (m^2/s) is the effective diffusivity (τ (-) is the tortuosity, and $D_v{}^0$ (m^2/s) is the binary diffusion coefficient of vapor). In Equation (3), ρ_m (kg/m^3), C_m (J/kg/K), and λ_m (W/m^2/K) are the effective density, specific heat capacity, and thermal conductivity of the medium, respectively. Effective properties of the medium are calculated based on the volume-averaged concept. C_l is the specific heat capacity of the liquid phase, and L_v (J/kg) is the latent heat of vaporization.

2.2. Hydraulic Constitutive Equations

The two important hydraulic constitutive relations are presented below:

2.2.1. Soil-water Retention Characteristics (SWRC)

In this study, non-isothermal Lu's SWRC model [53] is incorporated to analyze the non-isothermal multiphase flow. This SWRC model takes the capillary and adsorptive regimes into account. The adsorptive (θ_a) and capillary (θ_c) volumetric liquid contents are defined in the following equations:

$$\theta_l(\psi) = \theta_a(\psi) + \theta_c(\psi) \tag{4a}$$

$$\theta_a(\psi) = \theta_{a,\max}(T)\left\{1 - \left[\exp\left(\frac{\psi - \psi_{\max}}{\psi}\right)^M\right]\right\} \tag{4b}$$

$$\theta_c(\psi) = \frac{1}{2}\left[1 - \operatorname{erf}\left(\frac{\psi - \psi_{cav}}{\sqrt{2}\sigma_{cav}}\right)\right][n - \theta_a(\psi)]\left[1 + |\alpha\psi(T)|^{n_{VG}}\right]^{-m_{VG}} \tag{4c}$$

Where, $\theta_{a,\max}$ is the temperature-dependent maximum adsorption capacity and is defined as [54]: $\theta_{a,\max}(T)=\theta_{a,\max}(T_{ref})[1\text{-}c(T\text{-}T_{ref})]$. T_{ref} (K) is the reference temperature, and c (-) is a fitting parameter. In Equation 4(b), $\psi_{\max}$ (Pa) is the highest suction at which the volumetric liquid content reaches zero, and M (-) is the adsorption strength and depends on soil's type and adsorption capacity ($0<M<1$). In Equation 4(c), erf() is the error function; ψ_{cav} (Pa) is the mean cavitation suction and σ_{cav} (Pa) is the standard deviation and it is equal to $0.4\psi_{cav}$ in this study. Moreover, α (1/Pa), n_{VG}, and $m_{VG}=1\text{-}1/n_{VG}$ are VG model parameters. $\psi(T)$ is defined as [55]: $\psi(T)=[\sigma(T_{ref})/\ \sigma(T)]\ \psi(T_{ref})$. Where, σ (Pa/m) is the surface tension.

2.2.2. Darcy's Law

Liquid flow is governed by Darcy's law [Equation 5(a)] which is an empirical fluid flow model and traditionally considered in many numerical studies [52,56]. Please note that non-Darcy flow is based on the fact that at sufficiently high velocity there exists a non-linear relationship between flow rate and pressure [57]. In this study, special attention is given to the unsaturated hydraulic conductivity of the porous medium. The significance of film flow in the unsaturated flow condition has been discussed in previous studies [58]. Here, the permeability is comprised of the capillary ($k_{\text{int}}k_{rl}$ [m^2]), and film flow (k_{film} [m^2]) which is adopted from Zhang [59]. k_{int} [m^2] is the intrinsic permeability of the soil, and k_{rl} (-) is the relative permeability.

$$\mathbf{q_l} = -\frac{\rho_l \kappa_{unsat}}{\mu_l}\nabla(p_l + \rho_l g z) \tag{5a}$$

$$\kappa_{unsat} = \kappa_{\text{int}}\kappa_{rl} + \kappa_{film} \tag{5b}$$

$$\kappa_{rl} = \frac{\left\{1 - (\alpha\psi)^{n_{VG}-1}\left[1 + (\alpha\psi)^{n_{VG}}\right]^{\frac{1}{n_{VG}}-1}\right\}^2}{\left[1 + (\alpha\psi)^{n_{VG}}\right]^{\frac{n_{VG}-1}{2n_{VG}}}} \tag{5c}$$

$$k_{film} = f(1-n)\sqrt{2d_g}\pi^2\left(\frac{\varepsilon\varepsilon_0}{2\sigma}\right)^{1.5}\left(\frac{k_b T}{z_i a}\right)^3\left(1 + \frac{d_g\psi}{2\sigma}\right)^{-1.5} \tag{5d}$$

Where, μ_l (Pa.s) is the dynamic viscosity of the liquid, and g (m/s^2) is the acceleration of gravity. In Equation 5(c) k_{rl} is governed by the Mualem-van Genuchten relative permeability model and directly depends on the matric suction [60]. In Equation 5(d) (film flow equation), f is the dimensionless correction factor, where $f=1$ represents smooth uniform spherical grains. Moreover, d_g (m) is the effective grain diameter, ε=78.54 is the dimensionless relative permittivity of water, ε_0=8.85 $\times$ 10^{-12} (C^2/J/m) is the permittivity of free space, k_b=1.381 $\times$ 10^{-23} (J/K) is the Boltzmann constant, z_i =1 is the ionic charge, and a=1.602 $\times$ 10^{-19} (C) is the electron charge.

2.2.3. Non-equilibrium Phase Change

The mass phase change rate in the NEPC approach can be expressed as [61]:

$$\dot{m} = a_{lg}\kappa_{lg}(\rho_{v,eq} - \rho_v) \tag{6a}$$

$$\rho_{v,eq} = \rho_{v,sat}RH = \rho_{v,sat}\exp\left[\frac{\psi M_w}{RT\rho_l}\right] \tag{6b}$$

In Equation 6(a), a_{lg} (1/m) is the volume-normalized liquid-gas interfacial area, κ_{lg} (m/s) is the mass transfer rate coefficient, and $\rho_{v,eq}$ (kg/m^3) is the equilibrium vapor density. The equilibrium vapor density is defined in Equation 6(b) where RH (-) is the relative humidity governed by Kelvin's law. Moreover, R (Pa.m^3/K/mol) is the universal gas constant, M_w (kg/mol) is the molecular weight of liquid, and $\rho_{v,sat}$ (kg/m^3) is the temperature-dependent saturated vapor density.

Different mass phase change rates have been proposed in the literature for NEPC models [21]. In this study, a mass phase change rate based on the first-order macroscopic rate of kinetic mass transfer is considered:

$$\dot{m} = \theta_l K_{vap}(\rho_{v,eq} - \rho_v) \tag{7}$$

Where, K_{vap} (1/s) is the inverse of the time that is needed for the multiphase system to reach chemical equilibrium, and by increasing K_{vap}, the multiphase system reaches the equilibrium condition faster. Several efforts have been made in the literature to calculate K_{vap} [18,62]. It has been shown that K_{vap} is the function of volume-normalized liquid-gas interfacial area, pore gas volume, and vapor diffusivity [21]. The volumetric liquid content is included in Equation (7) to demonstrate the effect of the liquid mass per unit volume of the soil per time on the phase change rate. The preliminary results developed in this study confirm that adopting Equation (7) as the NEPC model provides accurate results despite its simplicity in which only one parameter (K_{vap}) needs to be calibrated. However, it is to be noted that more advanced models can be used instead of Equation (7), such as the Hertz-Knudsen-Schrage (HKS) model which requires multiple parameters to be calibrated [63–65].

2.2.4. Equilibrium Phase Change

The classical EPC model has been also utilized by many researchers to model the multiphase flow in the shallow subsurface soil [66,67]. To better express the difference of NEPC and EPC approaches, the results of both NEPC and EPC models are compared in the subsequent section where the developed numerical model of non-isothermal multiphase flow is validated with respect to the experimental in-field data. In the EPC approach for porous medium, the phase change is assumed to be instantaneous; therefore, it is a time-independent process. An advantage of this approach is that vapor density is equal to the equilibrium vapor density (i.e., $\rho_v = \rho_{v,eq}$) and is not solved independently. Hence, the matric suction and temperature are the only independent variables that need to be solved. By combining Equations (1) and (2), the balance equations for the EPC approach are as follows:

$$\text{Liquid Water} + \text{Water Vapor}: \rho_l\frac{\partial\theta_l}{\partial p_l}\frac{\partial p_l}{\partial t} + \nabla.(\mathbf{q}_l - D_v\nabla\rho_{v,eq}) = 0 \tag{8a}$$

$$\text{Balance of Energy}: (\rho C)_m\frac{\partial T}{\partial t} + \nabla.(\mathbf{q}_l C_l T - \lambda_m\nabla T) = -L_v\left[\frac{\partial\left(\theta_g\rho_{v,eq}\right)}{\partial t} + \nabla.\left(-D_v\nabla\rho_{v,eq}\right)\right] \tag{8b}$$

In equation 8(a), the temporal variation of equilibrium vapor density can be calculated from Equation 6(b); however, it is neg-

ligible in comparison to temporal variations of matric suction, and hence, it is disregarded. Moreover, the bracket in the right-hand side of Equation 8(b) presents the temporal and spatial variations of equilibrium vapor density to account for the latent heat of vaporization as it is frequently considered in the EPC approach [68].

2.2.5. Soil-atmosphere Boundary Condition

The complex heat, liquid, and vapor transport across the soil-atmosphere boundary are presented in this section for both EPC and NEPC approaches.

2.2.6. Liquid and Vapor Flow

Vapor flux, E (kg/m^2/s), and liquid flux (e.g., precipitation), P (kg/m^2/s), from the soil-atmosphere boundary can be evaluated from Equations 9(a) and (b), respectively.

$$P = \begin{cases} \rho_l P_a & p_l < 0\ (\psi > 0) \\ \rho_l R(H_a - H) & p_l \geq 0 (\psi = 0) \end{cases} \tag{9a}$$

$$E = \frac{1}{r_v}\left[\rho_v - (\rho_{v,eq})_a\right] \tag{9b}$$

Equation 9(a) is a mixed boundary condition that has been used in many studies and numerical software such as Hydrus-1D [69,70]. P_a (m/s) is the rate of precipitation from meteorological data, R (1/s) is the external resistance. Moreover, H_a (m) is the hydraulic head of the liquid water accumulate on the top of the soil-atmosphere boundary, and H=p_l /ρ_l /g (m) is the hydraulic head at the surface. When the soil's surface is in unsaturated condition, the liquid flux ($\rho_l P_a$) is triggered. However, when the soil's surface becomes saturated (or when reaches the infiltration capacity of the soil), either ponding or runoff may occur depending on H_a (m). H_a=0 represents the no ponding condition, which is assumed for the current model.

In Equation 9(b), ρ_v (kg/m^3) is the vapor density at the surface of the soil and $(\rho_{v,eq})_a$ (kg/m^3) is the equilibrium vapor density of air, at a reference height, z_{ref} (m), and r_v (s/m) is the equivalent aerodynamic resistant coefficient to the mass transfer, which serves as a sole vapor mass transfer coefficient. r_v is defined as follows [71,72]:

$$r_v = \frac{1}{\kappa^2 \upsilon}\left(\log\frac{z_{ref}}{z_0}\right)^2 (1+\delta)^{\nu} \tag{10a}$$

$$\delta = 5g\frac{(z_{ref} - d)(T - T_a)}{T_a \upsilon^2} \tag{10b}$$

$$\nu = \begin{cases} -2 & \delta < 0 \\ -0.75 & \delta > 0 \end{cases} \tag{10c}$$

Where, υ (m/s) and T_a (K) are the wind speed and air temperature recorded at the local station at the z_{ref} (m) height. Moreover, δ (-) is the atmospheric stability factor, κ=0.41 (-) is the von Karman constant, z_0 (m) is the surface roughness, and d (m) is a constant parameter which is equal to zero for bare soils. Equation 10(a) has an exact solution for atmospheric stable conditions and an approximate value with reasonable accuracy for unstable conditions [71].

2.2.7. Energy Balance Equation (EBE)

Heat exchange across the soil-atmosphere boundary is often formulated as [68]:

$$G = R_n - H - L_v E \tag{11a}$$

$$\begin{aligned} R_n &= R_{ns} + R_{nl} \\ &= (1-\alpha_{alb})S_n + \varepsilon_s \sigma_s \left\{\left[\left(1 - 0.84c_f\right)\varepsilon_a + 0.84c_f\right]T_a{}^4 - T^4\right\} \end{aligned} \tag{11b}$$

$$H = \frac{C_v}{r_H}(T - T_a) \tag{11c}$$

In Equation 11(a), G, R_n, and H (W/m^2) are the surface, net solar radiation, and sensible heat fluxes, respectively, and L_vE is the latent heat of evaporation from the top boundary. It is to be noted that the positive sign shows the incoming flux towards the soil surface and the negative sign represents the outgoing flux. In Equation 11(b), net radiation is decomposed to the net shortwave (R_{ns}) and the net longwave (R_{nl}) radiations. S_n (W/m^2) is the incoming solar radiation obtained from meteorological data. α_{alb}, ε_s are the surface albedo and soil surface emissivity, respectively, and σ_s=5.67 $\times$ 10^{-8} (W/m^2/K^4) is the Stefan-Boltzmann constant. Further, [(1 - 0.84c_f) ε_a + 0.84 c_f] is the atmospheric emissivity for cloudy sky, and c_f is the could factor [73]. The calculations of α_{alb}, ε_s, ε_a, and c_f are given in Appendix A. In Equation 11(c), C_v (=1200 J/m^3/K) is the volumetric heat capacity of the air, and r_H (= r_v) is the aerodynamic resistance to the heat transfer.

The hydro-thermal coupled interactions in the shallow subsurface and in the vicinity of a horizontal heat source are schematically presented in Fig. 1. Few centimeters below the soil-atmospheric boundary are highly affected by the atmospheric evaporative demand [26]. Precipitation may reach the deeper layers of the soil depending on the precipitation rate and soil's infiltration capacity. Close to the heat source, water evaporates around the heater, and the vapor transports to a further distance from the heater due to temperature and suction gradients wherein condenses to liquid water, and then the liquid water transports back to the heater through the thermally induced advection flow. Moreover, the heat transfers in the forms of conduction, convection, and latent heat. As the soil gets dryer around the heat source, the thermal conductivity of the soil gets reduced and, because of the lower water or vapor contents, heat conduction through the solid grains becomes the main heat transfer mechanism [47]. Different scenarios of non-isothermal multiphase flow in the shallow subsurface and close to a heat source are quantitively analyzed in the following sections.

It is to be noted that all the temperature-dependent and saturation-dependent parameters used in Equations (1) to (11) are expressed in Table 1. The rest of the temperature-dependent parameters are calculated from the formulations provided by the International Association for the Properties of Water and Steam (IAPWS 2007) [74].

2.3. Hydraulic and Thermal Properties of the Soil

In this section, the results obtained from the developed model are compared with the field test observations at a site near the University of California Agricultural Experimental Station in Riverside, CA [75]. According to Mohanty, Shouse and van Genuchten [75], the spatio-temporal variations of water content and temperature were measured using TDR probes and thermocouples, respectively, at two orthogonal transects, comprising 49 regularly spaced (1.0 m) sites. The measurements were obtained while the soil was subjected to artificial irrigation with a sprinkler system at different hours. The location of the field test is considered as an arid climate with large temperature fluctuation during a day, where the site of the study was flat and contains soil with a surface roughness of z_0 = 1 cm with no vegetation. The soil for this experiment was characterized as Arlington fine sandy loam (coarse-loamy, mixed, thermic Haplic Durixeralf) with an 8.8% clay fraction [68].

The accuracy of the calibrated NEPC model is investigated with respect to the measured temporal fluctuations of volumetric liquid water content and temperature at the 2, 7, and 12 cm below the soil surface. Then the results obtained from the NEPC model are

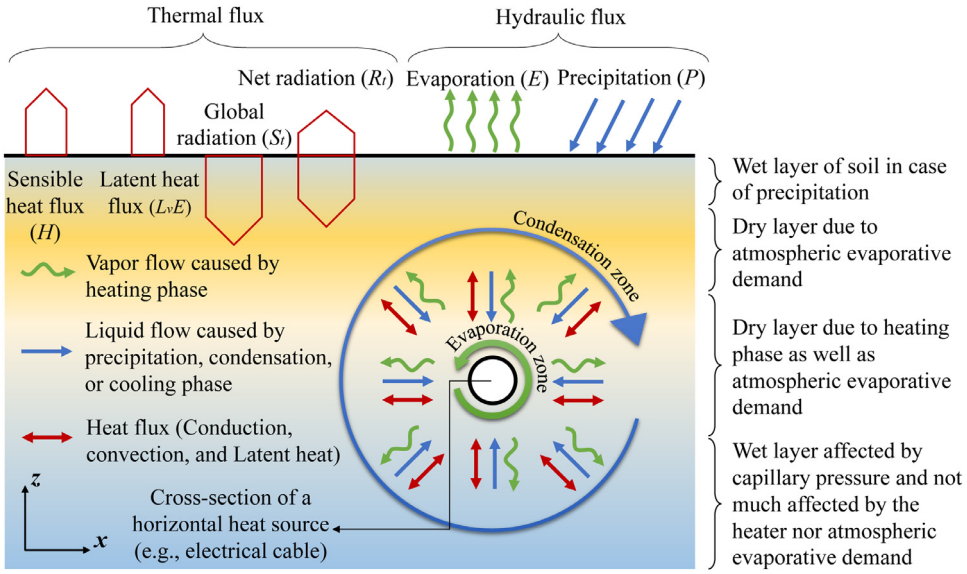

Fig. 1. A schematic overview of hydro-thermal processes in the shallow subsurface subjected to the environmental demand and in the vicinity of a horizontal heat source

Table 1
Dependent parameters used in non-isothermal multiphase flow equations

Parameter	Equation
Liquid Density [70]	$\rho_l = 1 - 7.37 \times 10^{-6}(T-4)^2 + 3.79 \times 10^{-8}(T-4)^3$
Saturated Vapor density [68]	$\rho_{v,sat} = 0.001T^{-1}\exp(31.37 - 6014.79T^{-1} - 0.00792T)$
Binary Vapor Diffusion Coefficient [68]	$D_v^0 = 2.92 \times 10^{-5}(T/273.15)^2$
Tortuosity [71]	$\tau = n^{-2}\theta_g^{7/3}$
Surface Tension [52]	σ =0.1177-0.0001535T
Latent Heat of Vaporization [72]	$L_v = 2.501 \times 10^6 - 2369.2(T + 273.15)$
Thermal Conductivity of the medium [68,73]	$\lambda_m = \frac{k_l\theta_l\lambda_l + k_g\theta_g\lambda_g + k_s(1-n)\lambda_s}{k_l\theta_l + k_g\theta_g + k_s(1-n)}$

Table 2
Hydraulic properties of Arlington fine sandy loam and the sandy loam from [54,75]

Soil	n (m^3/m^3)	$\theta_{a,max}$ (m^3/m^3)	K_s (cm/d)	n_{VG} (-)	α (1/m)	c (-)	ψ_{cav} (MPa)	ψ_{max} (MPa)	M (-)	f (-)	d_g^* (mm)
Arlington fine sandy loam	0.445	0.011	34.2	1.38	2.77	0.015	150	1000	0.35	50	0.02
Sandy loam	0.43	0.007	2.54	1.51	1.32	N/A**	150	1000	0.35	64	0.015

compared with the EPC model to highlight the difference in these two approaches. The meteorological data is obtained from the California Irrigation Management Information System (CIMIS) website (https://cimis.water.ca.gov/) from November 24th to December 5th, 1995. The reference height is equal to z_{ref} = 1.5 m.

First, the hydraulic and thermal responses of Arlington sandy loam are evaluated according to the data gathered from the literature [68,72,75]. For the sake of comparison, and to analyze the performance of the SWRC model, and HCF used in this study (Equation 5b) at higher matric suctions, the hydraulic data for a similar sandy loam is also considered in this study. All the parameters that are utilized to evaluate the SWRC and the HCF for both of these soils are presented in Table 2. The experimental data for Arlington fine sandy loam soil (Fig. 2a) are borrowed from Saito, Šimůnek and Mohanty [68] and the results for sandy loam soil (Fig. 2b, c, and d) are obtained from Pachepsky, Shcherbakov, Varallyay and Rajkai [76].

By referring to the data presented in Table 2 and implementing them in Equations 4(a)-(c) and 5(b)-(d), the SWRC and the HCF are illustrated in Figs. 2(a)-(d). Lu's and VG models are also compared in Figs. 2(a) and (b) for the two similar soils. As it can be seen, SWRC and HCF analytical models capture the experimental data with good accuracy. In addition, as can be seen in Figs. 2(c) and (d), the contribution of film flow in the overall hydraulic conductivity of the two soils is significant in matric suction values higher than 0.1 MPa.

The temperature- and saturation-dependent thermal conductivity of Arlington fine sandy loam is shown in Fig. 3 for different temperature levels. The detailed calculation of the thermal conductivity is discussed in Appendix B.

2.4. Validation of the Non-isothermal Multiphase Model

Two series of experimental data (two sites) are selected based on the original experiment that was conducted by Mohanty, Shouse and van Genuchten [75]. The duration of the experiment was from 24th November (Day of the Year [DOY] 328) to 5th December (DOY 339) in which irrigation was done on DOY 334 and 335. Because of the heterogeneity in the hydraulic properties of Arlington fine sandy loam for these sites, the porosity, and saturated hydraulic conductivity, are different for the two selected sites and these values for site 2 are, respectively, n = 0.416 m^3/m^3, and K_s = 31.31 cm/d. However, other parameters for site 2 are also according to Table 2 (site 1). Please note the complete experimental results for site 1 and site 2 are, respectively, borrowed from Saito, Šimůnek and Mohanty [68], and Sviercoski, Efendiev and Mohanty [72].

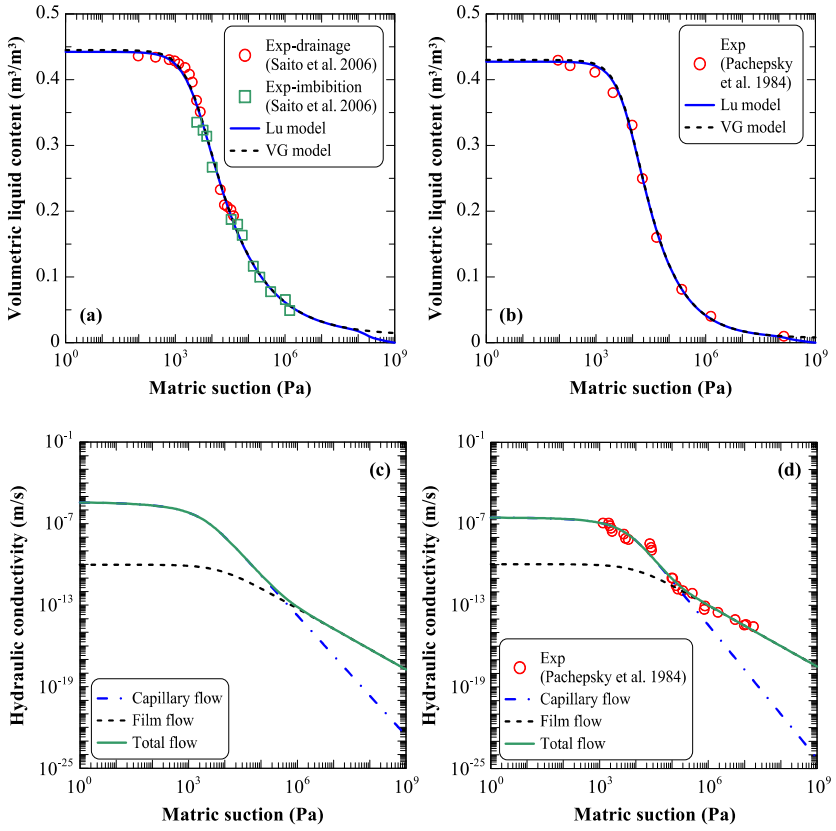

Fig. 2. The comparison of Lu (2016) and VG water retention curve models and capillary and film hydraulic conductivities used in this study with the experimental data for Arlington fine sandy loam and sandy loam

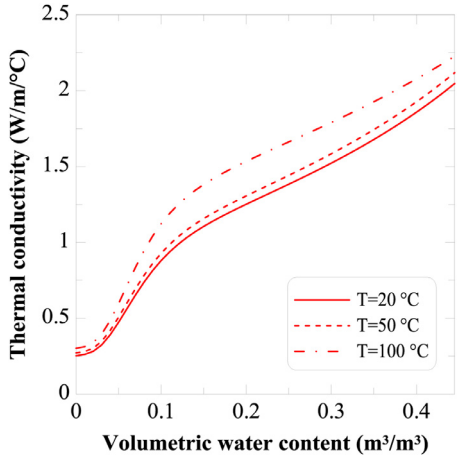

Fig. 3. The variability of thermal conductivity of the soil at different temperature and volumetric water content

1D simulations for the EPC and NEPC models are performed using COMSOL Multiphysics v5.3a where the length of the model (domain of the simulation) is 50 cm. The initial volumetric liquid content and the temperature of the domain are chosen based on the first experimental data points at different depths for each site. It is to be noted that the matric suction is back-calculated from the initial volumetric liquid content through the SWRC model. Moreover, the initial vapor density for the NEPC model is considered to be equal to the equilibrium vapor density. For the bottom boundary, thermal insulation and no-flow conditions are considered. For the soil-atmospheric boundary in NEPC approach, the boundary liquid flux [Equation 9(a)], the vapor flux [Equation 9(b)], and the heat flux [Equation 11(a)] are considered for the liquid mass balance [Equation (1)], the vapor mass balance [Equation (2)], and the energy balance [Equation (3)], respectively. For the EPC approach, boundary liquid and vapor fluxes [Equations 9(a) and (b)] are both imposed on the fluid mass balance [Equation 8(a)], and boundary heat flux is used for the energy balance in Equation 8(b). The meteorological data for evaluating the components of boundary liquid, vapor, and heat fluxes are presented in Appendix C. In addition, the precipitation rate for both sites is: P_s = 10.98 cm/d and is triggered for an hour on DOY 334.

Figs. 4 and 5 depict the variations of volumetric liquid content and temperature, respectively, obtained from the numerical model and experimental test at different depths for sites 1 and 2. The volumetric liquid content data at 2 cm is used to calibrate the inverse of equilibrium time which was found to be: K_{vap}=0.2 1/s. In general, if the evaporation rate from the soil or the fluctuation of moisture content and temperature in few centimeters close to the atmospheric boundary is known, the initially recorded data can be utilized to evaluate K_{vap}. Fig. 4 demonstrates that the difference between the results of EPC and NEPC approaches are quite pronounced for the liquid content fluctuations for both sites very close to the soil surface (e.g., at depth 2 cm below the surface) or after the irrigation at deeper depths (e.g., at the depth of 2 cm and 7 cm). However, there is no difference between these modeling approaches for 7 and 12 cm depths for the first six and a half days (before the irrigation). The EPC approach yields very strong and fast evaporation from the beginning of the experiment while the evaporation process in the NEPC model is smooth and is controlled by the rate of kinetic mass transfer in Equation (7). This observation has been stated by other researchers such as Smits, Cihan, Sakaki and Illangasekare [19] who compared the experimental evaporation rate from bare soil with the EPC and NEPC ap-

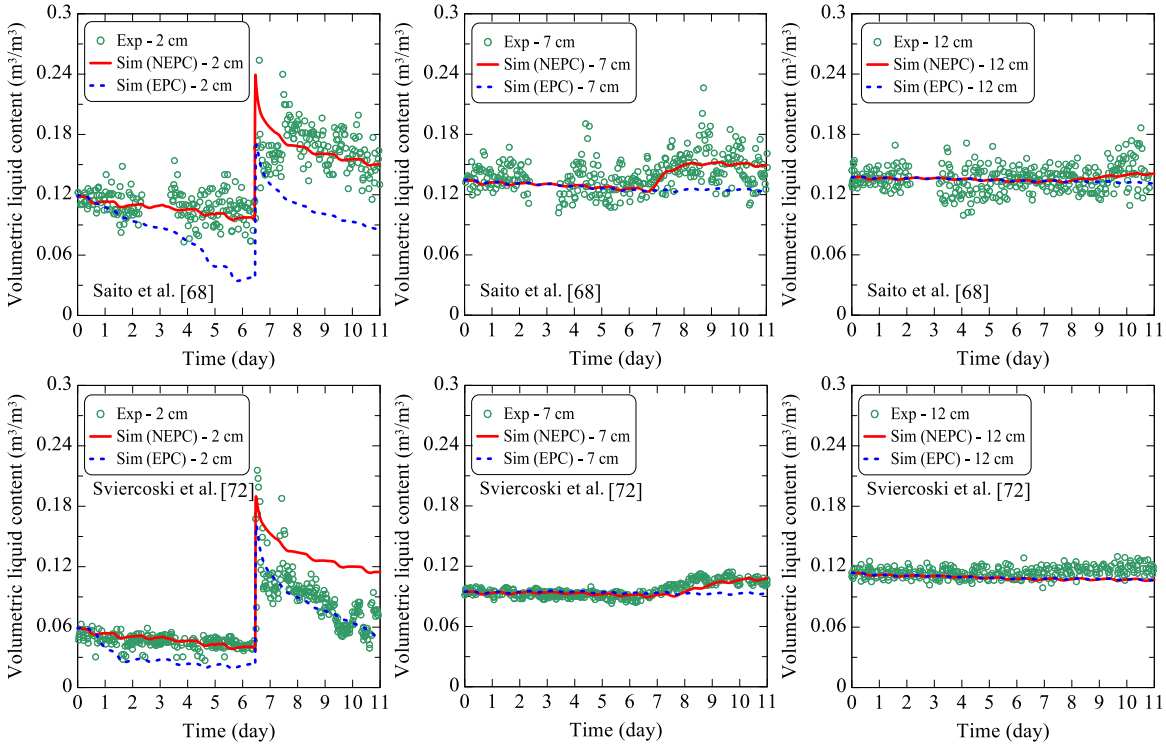

Fig. 4. The comparison of simulation (EPC vs. NEPC) and experimental results: Variations of volumetric liquid content at different depths for two different sites

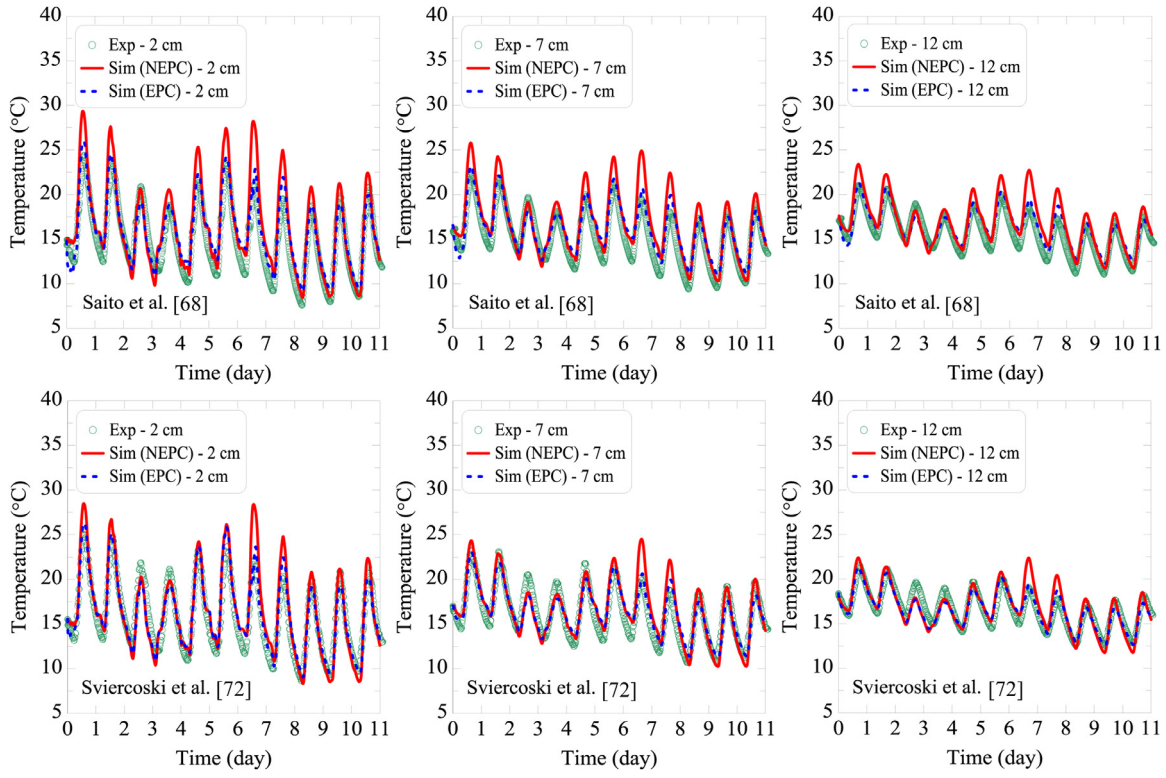

Fig. 5. The comparison of simulation (EPC vs. NEPC) and experimental results: Variations of temperature at different depths for two different sites

proaches. Please note, parameters such as the soil resistivity coefficient and the vapor enhancement factor are frequently incorporated in EPC and NEPC models [7,19]. The soil resistivity controls the rapid evaporation rate by decreasing the mass transfer coefficient in Equation 9(b). Additionally, the vapor enhancement factor is considered in the Fick's law of diffusion to increase the effective diffusivity, and consequently, the vapor transfer through the soil. However, these parameters are somewhat empirical and their validity has been questioned in previous studies [77]. Therefore, they are not included in the EPC and NEPC models that are presented in this study. The NEPC model only uses K_{vap} which can be evaluated experimentally and is constant for different initial saturation.

As mentioned earlier, according to the experimental result of volumetric liquid content at the depth of 2 cm, K_{vap} is calibrated to be 0.2 1/s. It is to be noted that, increasing the value of K_{vap}, mimics the equilibrium phase change condition. In particular, for $K_{vap} \geq 1000$ in this study, the modeling results for both EPC and NEPC approaches coincide (not shown here).

Fig. 5 shows the comparison of the soil temperatures at different depths measured in the field with the numerical results. As it can be seen in Fig. 5 the temperature dynamics of the soil are captured well with both the NEPC and EPC models at different depths for both sites which confirm the validity of the heat transfer model that is considered in this analysis. However, there are some discrepancies in the EPC and NEPC results at the maximum or minimum temperatures. This might be due to the fact that the EPC and NEPC models have a different heat source for vaporization (Please see the right-hand side of Equations (3) and 8(b) for the NEPC and EPC models, respectively).

All the components of the NEPC model have been evaluated and verified with the experimental observations. In the next section, the developed NEPC model is used to analyze the hydro-thermal responses of the unsaturated soil subjected to natural precipitation and evaporative demand at the soil surface while a horizontal heat source is buried in the shallow depth.

2.5. The Non-isothermal Multiphase in the Vicinity of a Horizontal Heat Source

2.5.1. The Description of the Symmetric 2D Model

The simulation of heat, vapor, and liquid flow in the vicinity of a horizontal heat source is considered here by utilizing the NEPC approach which is calibrated and validated against field test observations. The same location (Riverside, CA) and the same soil (Arlington fine sandy loam) are chosen as presented in the previous section which is subjected to a natural meteorological condition for a period of one year from September 30th, 2019 to September 30th, 2020. The atmospheric conditions including solar radiation, wind speed, relative humidity, temperature, and precipitation during the aforementioned one year are illustrated in Appendix C. The hydraulic data for Arlington fine sandy loam is also the same as the one presented in Table 2. The preliminary models confirm that the one-year modeling is adequate for the heat and mass flow caused by the evaporation and precipitation from the top boundary transfer deeper into the soil. In addition, a heat source with a radius of $D_p = 1.5$ cm is considered at $\boldsymbol{z} = -1.5$ m below the soil's surface. The radius of the heat source and the buried depth are chosen based on the buried electrical cables [45]. Moreover, due to the symmetrical geometry in the longitudinal direction (e.g., plain strain condition along the heat source), a 2D domain is selected to evaluate the heat and mass flow in vertical and horizontal directions. In addition, due to symmetry, only a half of the domain is modeled as shown in Fig. 6(a) to reduce the computational cost. The left side of the domain in Fig. 6 is the symmetric boundary.

The top boundary condition is governed by Equations 9(a), 9(b), and 11(a) for the liquid, vapor, and heat transport, respectively. Furthermore, the flow of heat, and vapor is prevented from the right and bottom boundaries: i.e., $(\nabla T)_{\boldsymbol{z}=-10} = (\nabla T)_{\boldsymbol{x}=10} = (\nabla \rho_v)_{\boldsymbol{z}=-10} = (\nabla \rho_v)_{\boldsymbol{x}=10} = 0$. The pore pressure for the bottom boundary is at the hydrostatic pressure and the liquid flow is disregarded on the right boundary: i.e., $(p_l)_{\boldsymbol{z}=-10} =$ <hydrostatic pressure> and $(\nabla p_l)_{\boldsymbol{x}=10} = 0$. Two thermal scenarios are imposed on the heat source. The first scenario consists of the only heating period in which a 20 W thermal power is turned on after 30 days and stays turned on thereafter. In the second scenario, periodic heating and cooling cycles are considered in which a 20 W thermal power is turned on after 30 days and stays on for 5 days (heating period) and then is turned off for the next 5 days (cooling or relaxation period). This cycle is maintained until the end of the simulation.

The domain is a 10 × 10 m square which is large enough to minimize the effect of bottom and right thermal and hydraulic boundaries on the area of interest around the heat source. The finite element discretization is done using quadratic elements with very fine mesh close to the soil-atmospheric boundary (top boundary) and the heat source boundary (the half-circle located on the left boundary). The total number of elements is 6166 after mesh sensitivity analysis. The initial temperature of the ground is considered 20.5 °C, and the initial matric suction is hydrostatic. The initial thermal and hydraulic conditions are obtained by performing a steady-state simulation (please see Fig. 6(b)). In addition, the initial vapor density is equal to its equilibrium value. Furthermore, the precipitation during the selected one year is also included in Fig. 6(c) which is imposed on the top boundary.

The main simulation is carried on, first, by analyzing the temperature and liquid content variations at different depths without considering the heat source (e.g., when the heat source is turned off). Then, the two scenarios of thermal heating and heating/cooling are applied. To better illustrate the effect of soil-atmospheric boundary condition on the thermo-hydraulic response of the soil in the presence of a heat source, two additional boundary conditions at the soil-atmospheric boundary are also taken into account and included when presenting the results.

3. Results and Discussion

Figs. 7 and 8 depict the temperature and volumetric liquid content fluctuations, respectively, for one year while the heater is turned off. To better compare the performance of the NEPC and EPC models, the simulation results obtained from the EPC approach are also included in Figs. 7 and 8. Further, the green circles in Fig. 7(b) are the experimental data obtained from the CIMIS website in which the soil's temperature is measured at the depth of 15 cm. The overall temperature variations obtained from the simulations are in reasonable agreement with the experimental observations. It is evident from Figs. 7(a) and (b) that, hourly fluctuations of the temperature at $\boldsymbol{z} = -2$ cm and $\boldsymbol{z} = -15$ cm are highly influenced by the atmospheric demand, whereas, as shown in Figs. 7(d) and (e), the rapid thermal changes in the atmospheric condition cannot swiftly disturb the temperature in deeper layers in soil (e.g., at the depth of 100 cm, or 150 cm). However, even for $\boldsymbol{z} = -1.5$ m, soil temperature fluctuates with changes in atmospheric temperature, and the maximum and minimum changes in the temperature are $\Delta T \approx +4.4$ and -5.2 °C for this particular time interval. As it was also evident from Fig. 5, the soil temperature obtained from the EPC approach also follows the same trend as obtained from the NEPC approach.

Variations of volumetric liquid content obtained from both NEPC and EPC models at different depths within one year before and after the precipitation are presented in Fig. 8. For the NEPC approach, Figs. 8(a) and (b) indicate that the evaporation and precipitation have an instant impact on the volumetric liquid content at the very shallow soil layers (e.g., at the depth of 2 cm and 15 cm). In particular, after the relatively heavier precipitation on the 163rd day [please see Fig. 6(c)], the maximum volumetric liquid content is reached at $\boldsymbol{z} = -2$ cm which is very close to the porosity of the soil (i.e., complete saturation). Moreover, Figs. 8(c)-(d) show that before the infiltration of excess liquid water from the precipitation to the lower depths, the evaporation from the soil surface does not alter the hydraulic response of the deeper soil layers. Nonetheless, the precipitation has a major impact on the saturation of the top couple of meters of the soil in the long term. As an example, at the $\boldsymbol{z} = -150$ cm, the maximum change in the volumetric liquid content is $\Delta\theta_l \approx 0.15$ m^3/m^3 and it happens when the precipi-

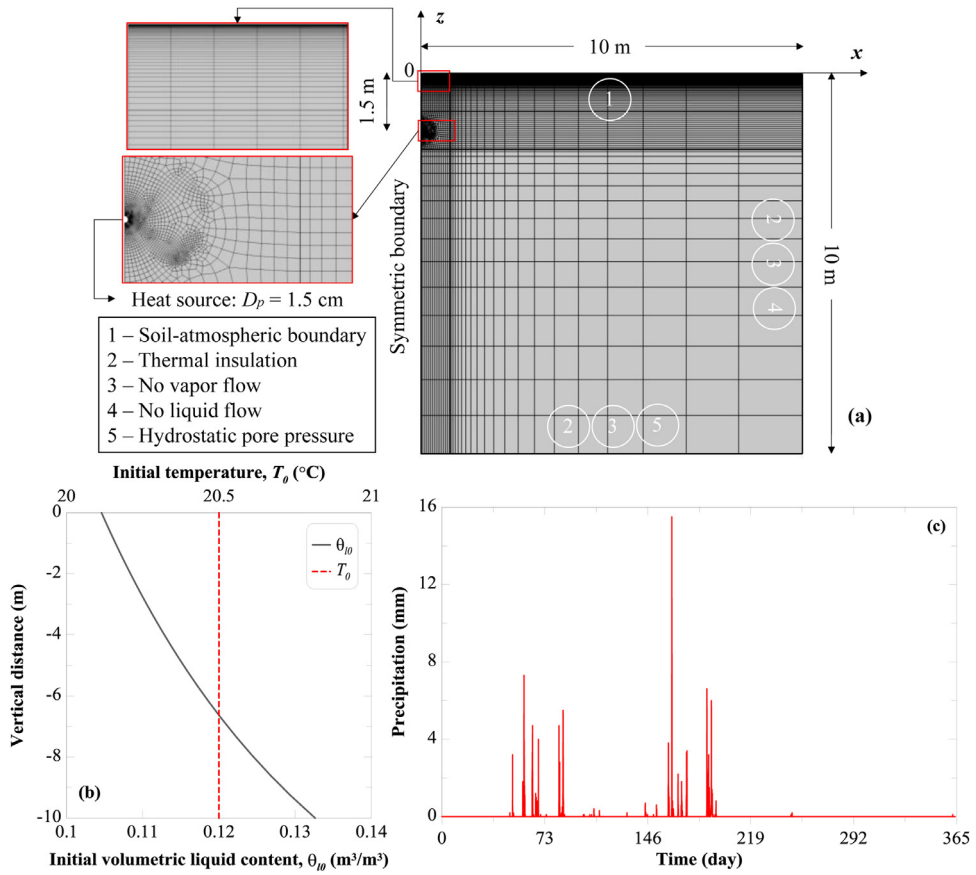

Fig. 6. (a) The schematic representation of the finite element discretization of the 2D domain, (b) thermo-hydraulic initial and boundary conditions, and (c) the precipitation obtain from meteorological data

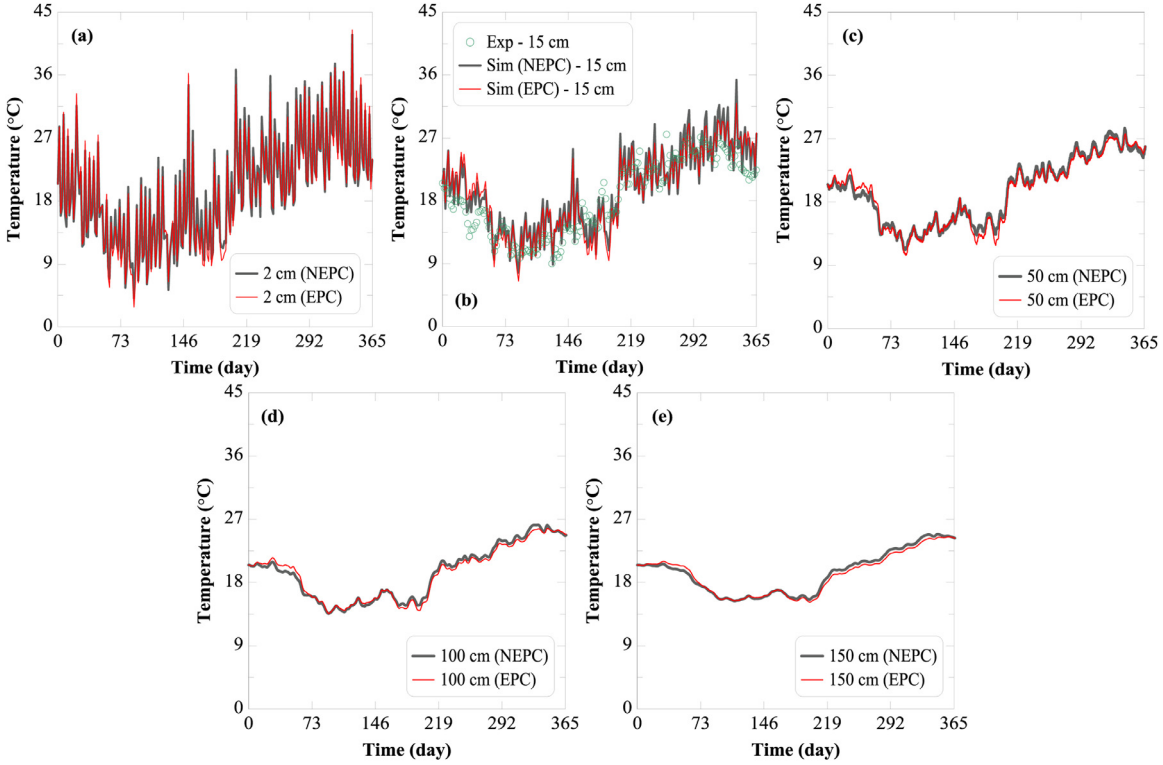

Fig. 7. Variations of temperature at different depths for one year where $x \in [0,10]$, and the heater is tuned off: (a) z = -2 cm, (b) z = -15 cm, and (c) z = -50 cm, (d) z = -100 cm, and (e) z = -150 cm below the soil-atmospheric boundary

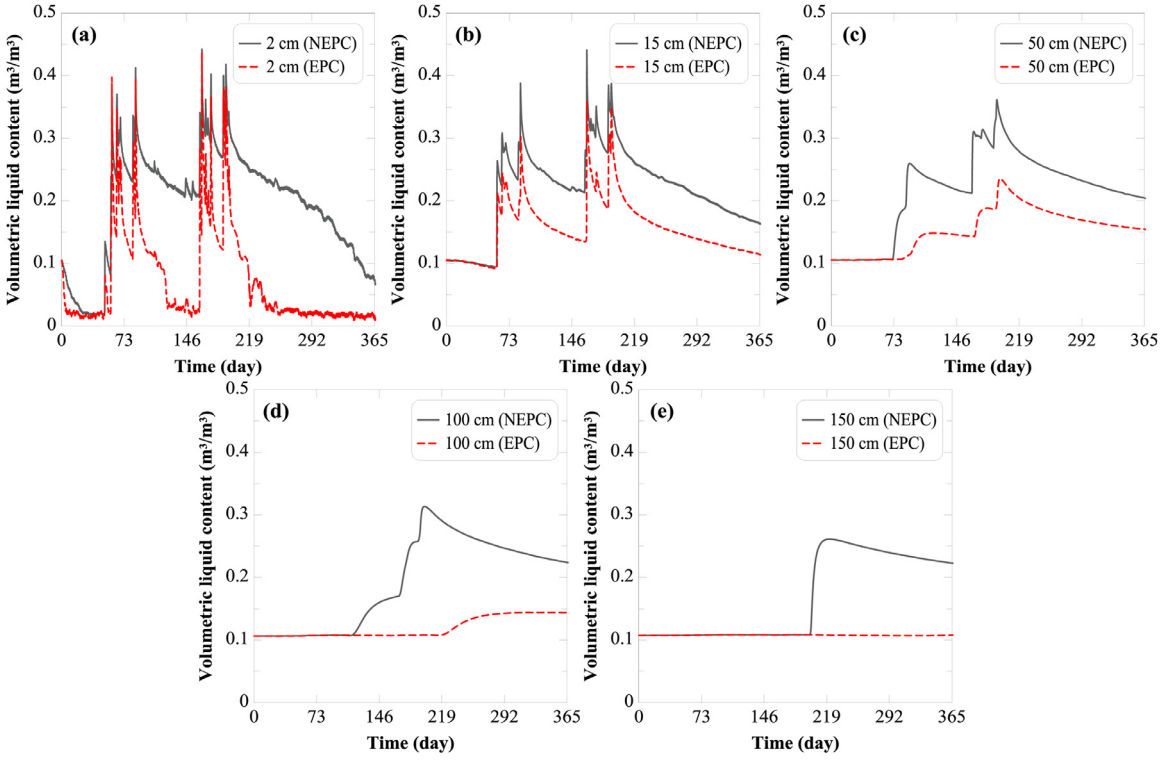

Fig. 8. Variations of volumetric liquid content at different depths for one year where $x \in [0,10]$, and the heater is tuned off: (a) z = -2 cm, (b) z = -15 cm, and (c) z = -50 cm, (d) z = -100 cm, and (e) z = -150 cm below the soil-atmospheric boundary

tation reaches this depth. In other words, about a 143% increase is observed in the liquid content with respect to its initial value which occurs on the 222nd day (almost two months after the prior precipitation event). The delay time in the infiltration depends on the soil's type, hydraulic conductivity, and the degree of saturation which dictate how fast water can flow through the soil medium.

In contrast to the NEPC model, the results obtained by the EPC approach show different behavior in the fluctuations of volumetric liquid content at different depths. The evaporation rate predicted by the EPC approach tends to be stronger than the NEPC approach. As it can be seen in Fig. 8(a), before the first precipitation event on the 48th day, the soil at 2 cm below the ground surface dries out faster in the EPC approach. The rapid-drying process is more evident after each precipitation event where the volumetric liquid content decreases much faster than the results obtained by the NEPC approach. The rapid-drying process in the EPC model happens because precipitation increases the volumetric water content and therefore, the evaporation is in its full potential due to a higher degree of saturation (e.g., more water availability for evaporation in the soil). Moreover, Figs. 8(b)-(e) demonstrate that before the first precipitation event, there is no difference between EPC and NEPC results for deeper soil layers as was also interpreted from the results in Fig. 4. However, it is interesting to note that after the precipitation, model predictions of EPC and NEPC approaches are largely different. This happens because the EPC model predicts fast and strong evaporation in the top few centimeters of the soil, and thus less water is available to infiltrate into the deeper layers. As a result, the EPC model shows no volumetric water change at z = -150 cm.

The results in Figs. 7 and 8 emphasize that the soil-atmospheric condition (evaporation and precipitation) in an arid area, such as the location chosen for this study, can significantly change the hydro-thermal conditions of both shallow subsurface soil (a few centimeters below the ground) and deeper soil layers. Therefore, it is necessary to accurately model the liquid, vapor, and heat flow across the soil-atmospheric boundary in an arid and semi-arid area. On the other hand, the results of the EPC approach show different impacts on the moisture fluctuations at both shallow and deeper soil layers. The difference in the equilibrium and non-equilibrium phase change is illustrated in Fig. 9 in terms of the latent heat source. The right-hand sides of Equations (3) and 8(b) are the latent heat sources for NEPC and EPC approaches, respectively. In Figs. 9(a) and (b), the latent heat source of the top 10 cm of the soil is shown at a specific time of the day for every two months, where the positive and negative values show the condensation and evaporation, respectively. It is important to note that the evaporation and condensation close to the soil surface are rapidly changing due to fluctuations in atmospheric demand. However, in Fig. 9 the changes of latent heat are shown only at a few time steps to compare the fundamental difference in EPC and NEPC approaches. The results in Fig. 9(a) state that only evaporation (negative latent heat source) occurs during the selected time steps in this figure. Please note, condensation occurs at different time steps which has not been shown in Fig. 9(a). It is interesting to note that, initially, the evaporation zone is wider and reaches z = -5 cm. After two months and when the resaturation of the top layer happens, the evaporation zone is closer to the ground. However, at later time steps because of the higher water availability (due to precipitation) in deeper layers of the soil, the magnitude and zone of evaporation gradually increase. However, after 12 months the total evaporation decreases due to lower water availability close to the soil surface while the evaporation zone increases because water infiltrates deeper into the ground. On the other hand, as it can be seen in Fig. 9(b), the phase change process obtained from the EPC approach is different. Initially, the evaporation is intense and largely close to the surface with a small amount of condensation in the deeper layers. In later times, condensation is evident in a wider layer beneath the soil-atmospheric

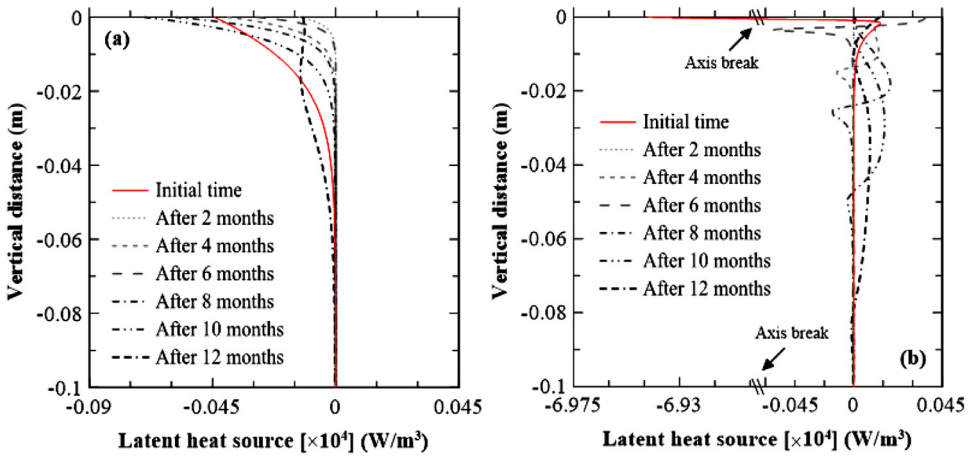

Fig. 9. Variations of latent heat source along the vertical distance below the soil-atmospheric boundary in the case where the heater is turned off: (a) NEPC, and (b) EPC

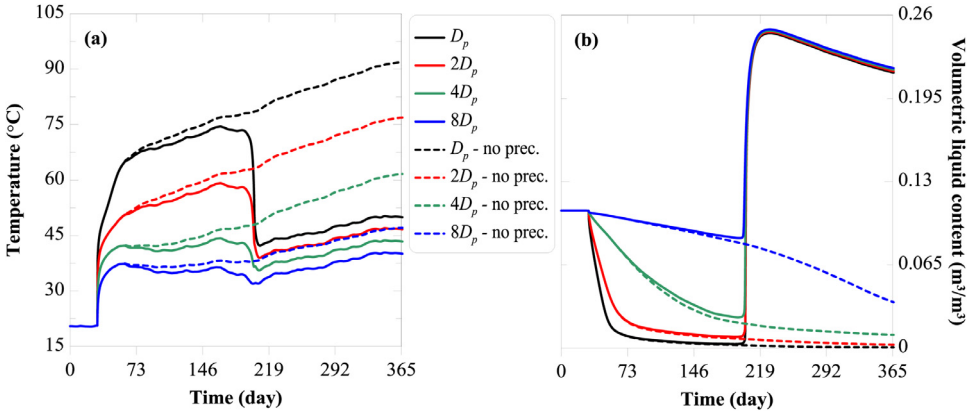

Fig. 10. Variations of (a) temperature, and (b) volumetric liquid content at different radial distances ($\boldsymbol{x} = D_p$, $2D_p$, $4D_p$, and $8D_p$) away from the heat source in the case of heating [$\boldsymbol{z}$ = - 150 cm] (solid lines: the top boundary is subjected to the evaporation and precipitation. Dashed lines: The precipitation is disregarded)

boundary, where in deeper layers evaporation takes place in a narrower region. The different behavior of evaporation/condensation in EPC and NEPC approaches directly affect the moisture distribution predicted by each model (please see Fig. 8). Therefore, previous observations by Smits, Cihan, Sakaki and Illangasekare [19] and Li, Vanderborght and Smits [20] can be completed which emphasize the importance of the NEPC approach over the EPC model. The concluding remark is that the NEPC model not only leads to capture the liquid, vapor, and heat flow in very shallow subsurface soil (e.g., within a few centimeters depth) but also is needed to accurately model the long-term moisture content variations in deeper soil layers when the soil surface is subjected to irrigation and/or precipitation. Therefore, in the next section, only the NEPC approach is utilized to analyze the thermo-hydraulic response of the porous medium close to an embedded heat source.

In the following, the focus is on the thermo-hydraulic process in the soil surrounding the horizontal heat source while the soil surface is subjected to both evaporation and precipitation. Figs. 10 and 11 compare the evolution of temperature and volumetric liquid content with time for different soil surface boundary conditions (e.g., no precipitation and no heat and mass flow boundary) at four points close to the heat source. As mentioned before, the heating phase starts after 30 days and stays turned on for the entire time at 20 W. The dashed lines in Figs. 10(a) and (b) show the results when no precipitation is allowed from the soil-atmospheric boundary: i.e., $(\nabla p_l)_{z=0} = 0$. The dashed lines in Fig. 11 show the results when neither heat transfer nor evaporation/precipitation is allowed from the soil-atmospheric boundary: i.e., $(\nabla T)_{z=0} = (\nabla \rho_v)_{z=0} = (\nabla p_l)_{z=0} = 0$. However, in both Figs. 10 and 11 solid lines present the base model in which the soil surface is subjected to both precipitation and heat flow (considering atmospheric demand).

The strongly coupled interactions between the thermal and hydraulic responses of the soil are evident in Fig. 10. In Fig. 10(a), the gradual increase in the temperature at different points close to the heat source can be observed until a drastic drop in the temperature occurs after about 200 days. The temperature at $\boldsymbol{x} = D_p$ is reduced by about 40%. The decrease in the temperature is directly correlated with the jump in the volumetric liquid content shown in Fig. 10(b). This coupled behavior can be interpreted through analysis of the saturation-dependent thermal conductivity which is used in this study. The heater, while turned on, is drying the surrounding soil which in turn decreases the thermal conductivity (as displayed in Fig. 3). Therefore, for the low thermal conductivity of the soil medium, the ability to conduct heat to a further distance is reduced. Consequently, the heat accumulates in the soil close to the heater. After the sudden resaturation, due to the infiltrated liquid water, the thermal conductivity rapidly increases and facilitates the heat conduction. Hence, the accumulated heat is released and flows to further distances. After the decrease in temperature, the results in Fig. 10(a) show the second increase in temperature which, again, is directly due to the gradual decrease in the volumetric liquid content due to heat-induced drying close to the heater. These observations mark the importance of the saturation-

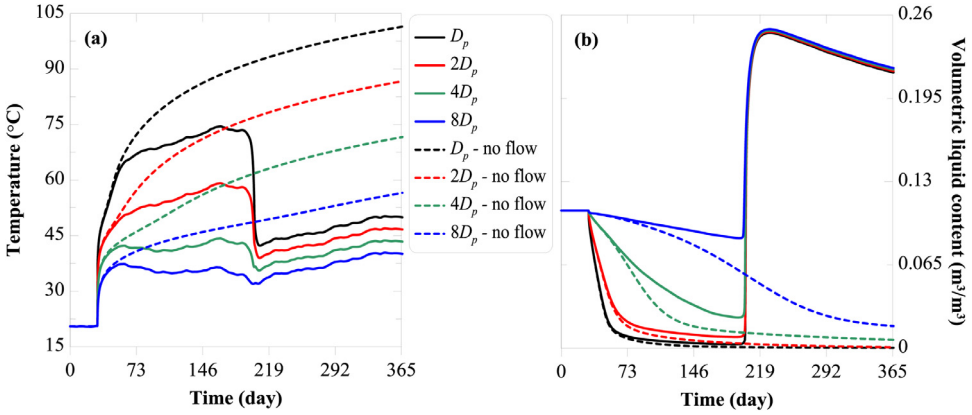

Fig. 11. Variations of (a) temperature, and (b) volumetric liquid content at different radial distances ($\boldsymbol{x} = D_p$, $2D_p$, $4D_p$, and $8D_p$) away from the heat source in the case of heating [$\boldsymbol{z}$ = -150 cm] (solid lines: the top boundary is subjected to the evaporation and precipitation. Dashed lines: heat, vapor, and liquid flow is ignored from the top boundary)

dependency of thermal conductivity to analyze the non-isothermal multiphase flow in soil.

Figs. 10(a) and (b) demonstrate slightly higher temperature and lower volumetric liquid content for the case of no precipitating after the heater is turned on. In this case and in the absence of liquid resaturation, the evaporation which is triggered by the heater dries out the surrounding soil and the thermal conductivity of the soil medium is gradually decreased. Comparably, the same situation happens close to the heat source. However, in the case of precipitation, when the shallow depths of the soil are infiltrated by the liquid water, the thermal conductivity is recovered, and consequently, facilities the heat flow. In conclusion, the overall conductive heat flux, in case of no precipitation, is lower than the case where precipitation takes place which results in higher temperature for soils close to the heater. This situation is even more pronounced in a case where no heat, vapor, and liquid flow is allowed from the top surface (because of the thermal insulation from the top boundary the heat accumulates close to the heater) [Figs. 11(a) and (b)]. In this case (no flow condition at the top surface), the heater is the only thermal load that desaturates the surrounding soil, and at the same time, the thermal conductivity is decreased which leads to lower conductive heat flux in the medium and higher temperature close to the heat source. After 200 days, the desaturation and the steady increase in temperature are continued and proceeded to further locations away from the heat source in case of no precipitation and/or no-flow conditions. The results in Figs. 10 and 11 emphasize the significance of the soil-atmospheric boundary to accurately predict the heat and fluid flow even on the deeper soil layers when dealing with an internal heat source (e.g., buried electrical cables).

Variations of heat and volumetric liquid content (for every two months) are shown in Fig. 12 along the horizontal distance away from the heat source for two cases of heat and mass flow from the soil-atmospheric boundary (base analysis) and no-flow conditions (no heat nor liquid flow). By comparing the results in Figs. 12(a) and (b), it is evident that the dynamic atmospheric condition not only affects the magnitude of temperature evolution emitted from the heat source but also has a notable impact on the thermal influence zone in the vicinity of the heater. In Fig. 12(a), the temperature rises to $\boldsymbol{x}$ = 3 m in the horizontal direction after 2 months (one month after the heater is turned on) and reaches $\boldsymbol{x}$ = 4.5 m after 8 months regardless of the maximum temperature drop (which occurs close to the heat source) due to resaturation. It is to be noted that the negative temperature variations ($\Delta T_{max} \approx$ -5 °C) at farther zones after 6 months are the result of cooling effects from the atmospheric demand. On the other hand, in the case of disregarding the atmospheric demand (i.e., a no-flow condition in Fig. 12b), the thermal influence zone progressively increases from $\boldsymbol{x}$ = 3 m after 2 months to $\boldsymbol{x}$ = 9 m after 12 months while the maximum temperature is also increasing monotonically.

Figs. 12(c) and (d) illustrate the dry-out zone in the vicinity of the heat source. The sharp decrease in the volumetric liquid content takes place after 2 months as shown in Fig. 12(c), and the dry-out zone is intensified up to 6 months due to the higher temperature built-up. However, the disturbance in the volumetric liquid content is limited to $\boldsymbol{x}$ = 0.5 m from the beginning of the heating phase. When resaturation occurs, the heat source cannot dry out the soil as strongly as in the case of low saturation which is due to the facilitated heat transfer and, consequently, lower temperature built-up close to the heat source. However, in Fig. 12 (d) since no resaturation occurs in case of no-flow condition from the soil's surface, the dry-out zone is continuously intensified. Therefore, it can be concluded that the coupled interactions between thermal and hydraulic processes in the soil are crucial to identify the zones where sharp reduction in moisture content happens to accurately design the buried electrical cables and horizontal heat exchanger tubes [44].

Figs. 13(a) and (b) present the variations of temperature and volumetric liquid content in the top 3 meters (-3 m $\leq \boldsymbol{z} \leq$ 0 m). Similar results are evident as were shown in the previous figure but in the case of vertical distance. In the top 1.5 meters in Fig. 13(a), which is the vertical distance between the heat source and the soil-atmospheric boundary, the evolution of temperature is strongly affected by both atmospheric demand and the heater. This observation is rational as it has already been established from Fig. 7(c) that highly dynamic heating/cooling phases imposed by the atmospheric condition can reach at least a couple of meters below the soil's surface and change the temperature field in the soil. In contrast, the moisture content variations, due to evaporation and condensation forced by the atmospheric condition, can only be seen for the top few centimeters of the soil. The water infiltration due to precipitation, however, can reach to few meters below the ground which is also evident from Fig. 13(b). For example, after 12 months the water reaches down to about $\boldsymbol{z}$ = -3 m (1.5 m below the heat source). Long-term and time-dependent monitoring and simulation of heat and fluid flow with respect to the atmospheric demand are of paramount importance which should be carefully taken into account in the modeling and design of buried heat sources.

The effect of heating/cooling cycles from a buried heat source on the thermo-hydraulic response of the soil is discussed in Figs. 14 and 15. The heating/cooling cycles are started after 30 days for

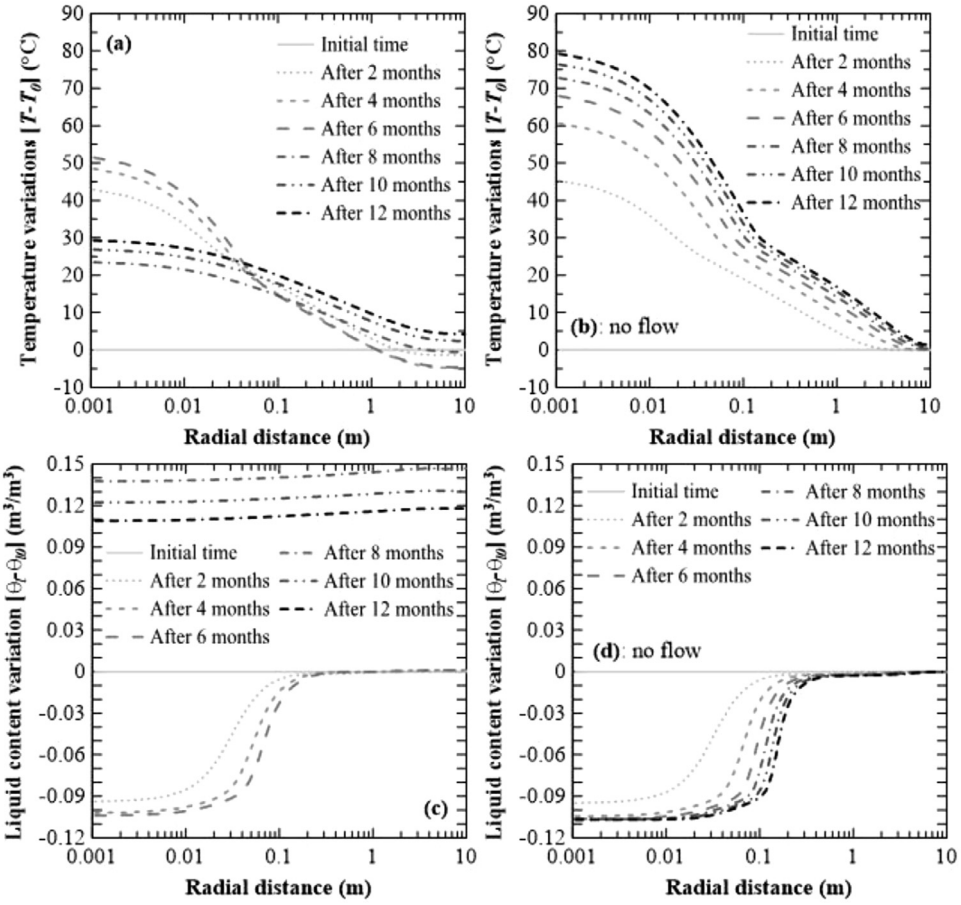

Fig. 12. Variations of temperature [(a) and (b)] and volumetric liquid content [(c) and (d)] with respect to the radial distance away from the heat source (z = -150 cm) for every two months: For (a) and (c), the top boundary is subjected to the evaporation and precipitation. For (b) and (d), heat, vapor, and liquid flow are prevented from the top boundary [$(\theta_{l0})_{z=-1.5\ m} = 0.107\ m^3/m^3$] – All results are shown for heating phase

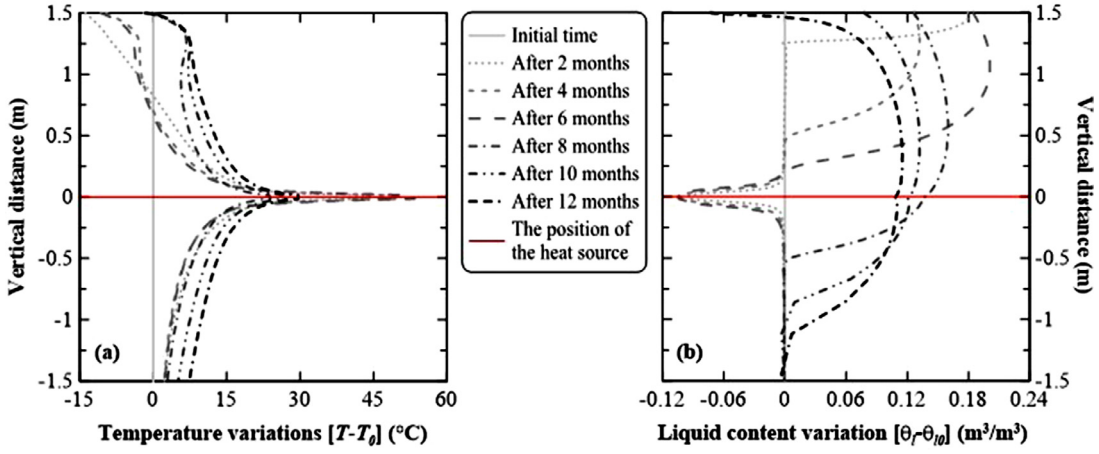

Fig. 13. Variations of (a) temperature and (b) volumetric liquid content with respect to the vertical distance away from the heat source ($x = D_p$) for every two months – All results are shown for heating phase

every 10 days in which the first 5 days are the heating period at 20 W and the subsequent 5 days are the cooling (relaxation) period in which the heater is turned off. Figs. 14(a)-(d) present the wave-like thermal fluctuations at different points close to the heat source for two cases of considering atmospheric demand and no-flow conditions. In the case of the no-flow condition, heating/cooling cycles lead to a gradually higher temperature especially close to the heat source. The amplitude of the cycles is smaller at points further from the heat source. In the case where atmospheric demand is imposed, except for the temperature at $x = D_p$ and $2D_p$, there is a gradual decrease in the temperature dynamic before the re-saturation event at 200 days. It is evident that the sudden drop in the temperature due to the increase in the degree of saturation is not as strong as the case where the constant heating phase was

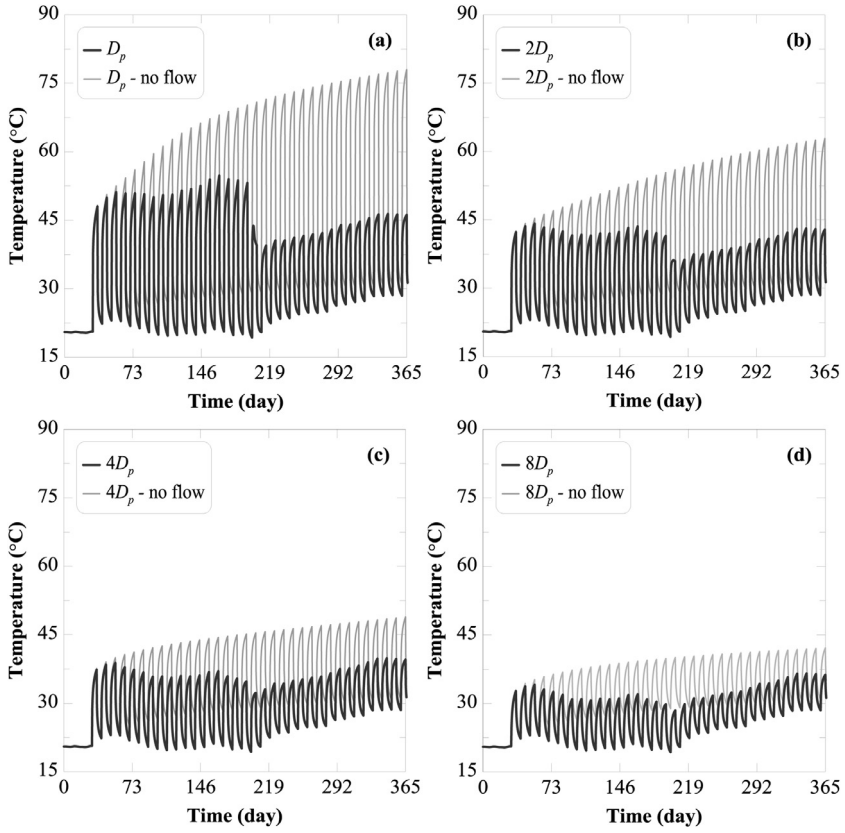

Fig. 14. Variations of temperature at different radial distance away from the heat source [z = -150 cm] during heating/cooling periods: (a) $x = D_p$, (b) $2D_p$, (c) $4D_p$, and (d) $8D_p$ (solid lines: The top boundary is subjected to the evaporation and precipitation. Dashed lines: heat, vapor, and liquid flow is ignored from the top boundary)

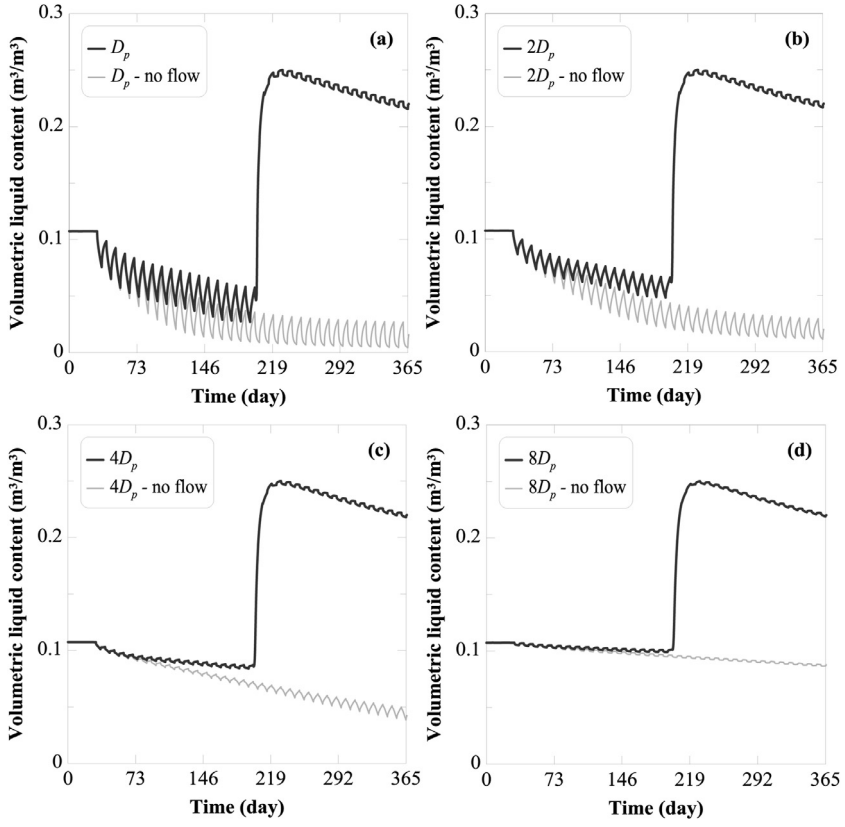

Fig. 15. Variations of volumetric liquid content at different radial distance away from the heat source [z= -150 cm] during heating/cooling periods: (a) $x = D_p$, (b) $2D_p$, (c) $4D_p$, and (d) $8D_p$ (solid lines: The top boundary is subjected to the evaporation and precipitation. Dashed lines: heat, vapor, and liquid flow is ignored from the top boundary)

considered [Fig. 10(a)]. Moreover, the higher degree of saturation leads to lower, but still notable, heating/cooling cycles' amplitude in which the temperature is progressively increased.

Figs. 15(a)-(d) demonstrate the volumetric liquid content fluctuations in the vicinity of the heat source at different points. The local drying/wetting cycles are directly influenced by the heating/cooling cycles. In Fig. 15(a) and for the case of the no-flow condition, despite the fact that constant heating/cooling is applied, the drying/wetting cycles are not completely reversible, and a moderate drying exists until a steady drying/wetting cycle is reached after 300 days. The same statement can be made for Fig. 15(b); however, the steady-state drying/wetting cycles are reached at a later time with a slower pace at $\boldsymbol{x} = 2D_p$. In Figs. 15(c) and (d), gradual drying is also observed but with a much weaker rate. It should be noted that the deviation of the results of no-flow condition from the case in which the atmospheric demand is considered occurs after 3, 4, 5, and 6 cycles for $\boldsymbol{x} = D_p$, $2D_p$, $4D_p$, and $8D_p$, respectively. In Figs. 15(a)-(d), after 200 days when resaturation happens, the amplitude of drying/wetting cycles is significantly smaller regardless of the distance to the heater. The comparison of this observation with fluctuation in temperature after resaturation illustrates the fact that in a higher degree of saturation the heating/cooling cycles result in lower temperature ranges (lower amplitude), and consequently, have a lesser phase change effect on moisture dynamics.

4. Conclusion

The non-isothermal multiphase flow, when soil is subjected to external (i.e., atmospheric demand) and an internal heat source (e.g., electrical cables), is of paramount importance to understanding the thermo-hydraulic response of soils. In this study, the non-equilibrium phase change model (NEPC) is utilized to simulate heat, liquid, and vapor transport in shallow subsurface soil when a horizontal heat source is presented. The developed model in this study is compared and validated with the experimental observation and the classical equilibrium phase change (EPC) model. In the main study, the non-isothermal multiphase flow is simulated based on EPC and NEPC models for one year under real meteorological conditions. The EPC and NEPC models simulated somewhat similar variations of temperature due to the atmospheric demand at different depths. However, the NEPC approach predicted large variations of moisture content at deeper soil layers due to water infiltration, while the EPC approach provided different results in which the infiltrated water could not reach deeper depths due to strong and rapid evaporation at the soil surface. Next, the thermo-hydraulic response of soil surrounding an embedded heat source in the vadose zone was analyzed while considering different thermal loadings. Thermal conductivity is found to be the major coupling factor in the thermo-hydraulic process. The high dependency of hydraulic conductivity was shown through the large variations in the degree of saturation which was controlled by the infiltration of precipitation into the soil. The dynamic of atmospheric demand with respect to the temperature and the precipitation is another significant factor that directly influences the thermo-hydraulic response of the soil close to a heater in shallow subsurface soil and should be considered carefully. The numerical results demonstrate that the increase in moisture content (due to precipitation) in few meters of the shallow subsurface significantly facilitates the heat transfer in the medium and enhances the heat dissipation away from the heat source. Higher heat transfer rate in the medium results in about 40% to 50% reduction in soil temperature close to the heat source. It was also observed that when the soil is initially in low saturation condition the drying zone surrounding the heat source is more intense, due to the stronger thermally-induced vapor diffusion in soils with lower moisture content. However, in high and intermediate saturation conditions that happen after precipitation events, the drying process around the heater is less pronounced. The long-term thermo-hydraulic response of the embedded heat source determines that cyclic heating-cooling thermal loads contribute to gradually drying the soil by 85%, 75%, and 50% respectively, at $\boldsymbol{x}=D_p$, $2D_p$, $4D_p$ from the heater when there is no precipitation. It is worth noting that the theoretical model developed in this study can also be extended to incorporate the mechanical deformation of soil and account for porosity changes which is important for fine-grain soils such as clays.

Declaration of Competing Interest

The authors declare that they have no known competing financial interests or personal relationships that could have appeared to influence the work reported in this paper.

CRediT authorship contribution statement

Mohammadreza Mir Tamizdoust: Resources, Conceptualization, Methodology, Software, Formal analysis, Investigation, Data curation, Writing – original draft, Writing – review & editing. **Omid Ghasemi-Fare:** Project administration, Conceptualization, Methodology, Supervision, Data curation, Funding acquisition, Writing – original draft, Writing – review & editing.

Acknowledgments

The authors would also like to gratefully acknowledge the financial support by the National Science Foundation under Grant No. CMMI-1804822.

Appendix A

According to Bittelli, Campbell and Tomei [73], the surface albedo and soil's surface emissivity are formulated as below:

$$\begin{cases} \alpha_{alb} = 0.25 & \theta_{l,top} < 0.1 \\ \alpha_{alb} = 0.1 & \theta_{l,top} < 0.25 \\ \alpha_{alb} = 0.35 - \theta_{l,top} & 0.1 \le \theta_{l,top} < 0.25 \end{cases} \tag{A1}$$

$$\varepsilon_s = \min\left(0.90 + 0.18\theta_{l,top}; 1.0\right) \tag{A2}$$

Where they both depend on the surface volumetric liquid content, $\theta_{l,top}$. Moreover, atmospheric emissivity is defined as:

$$\varepsilon_a = 0.70 + 5.95 \times 10^{-5} e_a \exp\left(\frac{1500}{T_a}\right) \tag{A3}$$

$$e_a = 0.611 \exp\left[\frac{17.27(T_a - 273.15)}{T_a - 35.85}\right] RH_a \tag{A4}$$

T_a (K) is the air temperature. e_a (kPa) is the atmospheric vapor pressure, and RH_a is the relative humidity of the air. The cloud factor is calculated from the atmospheric transmission coefficient for solar radiation, T_t:

$$0 \le c_f = 2.33 - 3.33T_t \le 1 \tag{A5}$$

$$T_t = \frac{S_n}{Q_p}; Q_p = 1360 \cos\theta \left[\frac{\mathrm{W}}{\mathrm{m}^2}\right] \tag{A6}$$

Table B1
Dependent parameters for the thermal conductivity of the porous medium [73] (T [°C])

Parameter	Equation
Thermal conductivity of water	$\lambda_l = 0.56 + 0.0018T$
Thermal conductivity of air	$\lambda_a = 0.0242 + 0.00007T$
Saturation vapor pressure	$p_{v,sat} = 0.611\exp(\frac{17.502T}{T+240.97})$
Slope of the saturation vapor pressure function	$\Delta = \frac{\partial p_{v,sat}}{\partial T}$
Molar density of air	$\bar{\rho}_a = 44.65\frac{273.16}{T+273.16}[\frac{\text{mol}}{\text{m}^3}]$
Actual vapor pressure	$e_a = \max\{1 - \frac{p_{v,sat}}{p_a}, 0.3[\text{kPa}]\}$

*Estimated based on hydraulic conductivity (K_s) using Kozeny-Carman model [76]
**Not Applied

Q_p is the potential daily global solar radiation, and θ is solar elevation zenith angle which is given by:

$$\cos\theta = \sin\lambda\sin\delta + \cos\lambda\cos\delta[0.2618(t - t_0)] \tag{A7}$$

$$\sin\delta = 0.3985\sin\left[2\pi\frac{\text{DOY}}{365} - 1.414 + 0.03345\sin\left(6.224 + \pi\frac{\text{DOY}}{365}\right)\right] \tag{A8}$$

In Equation (A7), λ is the latitude, δ is the solar declination, t is time and t_0 is the time of solar noon. DOY represents a day of the year.

Appendix B

The thermal conductivity function that is used in this study is originally proposed by Philip and De Vries [16], modified by Campbell, Jungbauer Jr, Bidlake and Hungerford [78], and completed by Bittelli, Campbell and Tomei [73]. In the thermal conductivity equation shown in Table 1, λ_g, λ_s and λ_l are thermal conductivities of gas, solid and liquid, respectively. λ_s=4.5 W/m/K is assumed in this study. In addition, k_g, k_s and k_l are weighting factors for gas, solid and liquid, respectively:

$$k_g = \frac{1}{3}\left[\frac{2}{1 + \left(\frac{\lambda_g}{\lambda_f} - 1\right)g_a} + \frac{1}{1 + \left(\frac{\lambda_g}{\lambda_f} - 1\right)g_c}\right] \tag{B1}$$

$$k_s = \frac{1}{3}\left[\frac{2}{1 + \left(\frac{\lambda_s}{\lambda_f} - 1\right)g_a} + \frac{1}{1 + \left(\frac{\lambda_s}{\lambda_f} - 1\right)g_c}\right] \tag{B2}$$

$$k_l = \frac{1}{3}\left[\frac{2}{1 + \left(\frac{\lambda_l}{\lambda_f} - 1\right)g_a} + \frac{1}{1 + \left(\frac{\lambda_l}{\lambda_f} - 1\right)g_c}\right] \tag{B3}$$

In Equations (B1)-(B3), g_a and g_c are shape factors. According to [73], g_a = 0.088 and g_c = 1-2 × g_a for mineral soils. Furthermore, λ_f is the fluid thermal conductivity:

$$\lambda_f = \lambda_g + f_w(\lambda_l - \lambda_g) \tag{B4}$$

where f_w is an empirical parameter:

$$0 \le f_w = \frac{1}{1 + \left(\frac{\theta_l}{\theta_0}\right)^{-q}} \le 1 \tag{B5}$$

$$\begin{cases} q = 7.25m_y + 2.52 \\ \theta_0 = 0.33m_y + 0.078 \end{cases} \tag{B6}$$

The values of 0 and 1 for f_w are representing dry and saturated soil conditions, respectively. m_y is the fractional clay content. In Equation (B4), the thermal conductivity of gas, λ_g, is calculated from:

$$\lambda_g = \lambda_a + \frac{L_v\Delta f_w\bar{\rho}_a D_v^0}{p_a - e_a} \tag{B7}$$

p_a is the atmospheric pressure (=1 bar). Other components of Equation (B7), as well as the rest of the parameters that used to calculate the thermal conductivity, are presented in Table B1:

Appendix C

The meteorological data which is obtained from the CIMIS website for the validation and long-term simulations are presented below:

A) Validation (1D model):
Fig. C1
B) Symmetric 2D model (Sep. 2019 – Sep. 2020):
Fig. C2

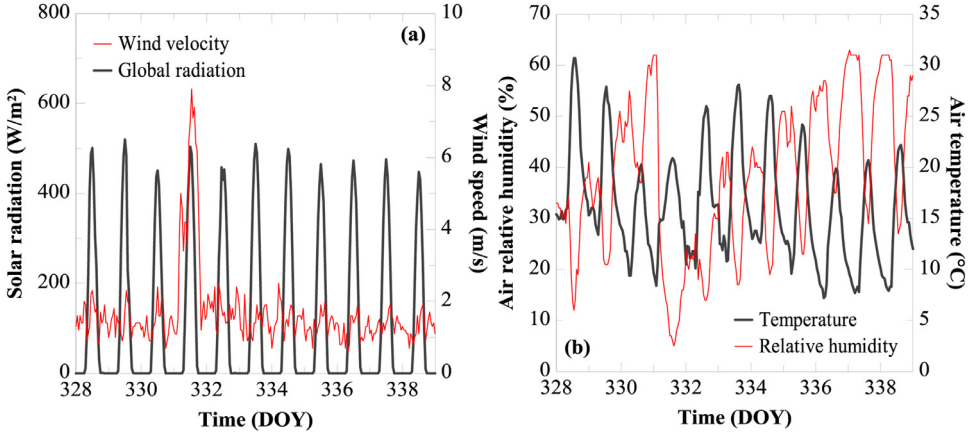

Fig. C1. The meteorological data used to simulate the atmospheric condition for the validation model: (a) Solar radiation and wind velocity, and (b) relative humidity and temperature of the air

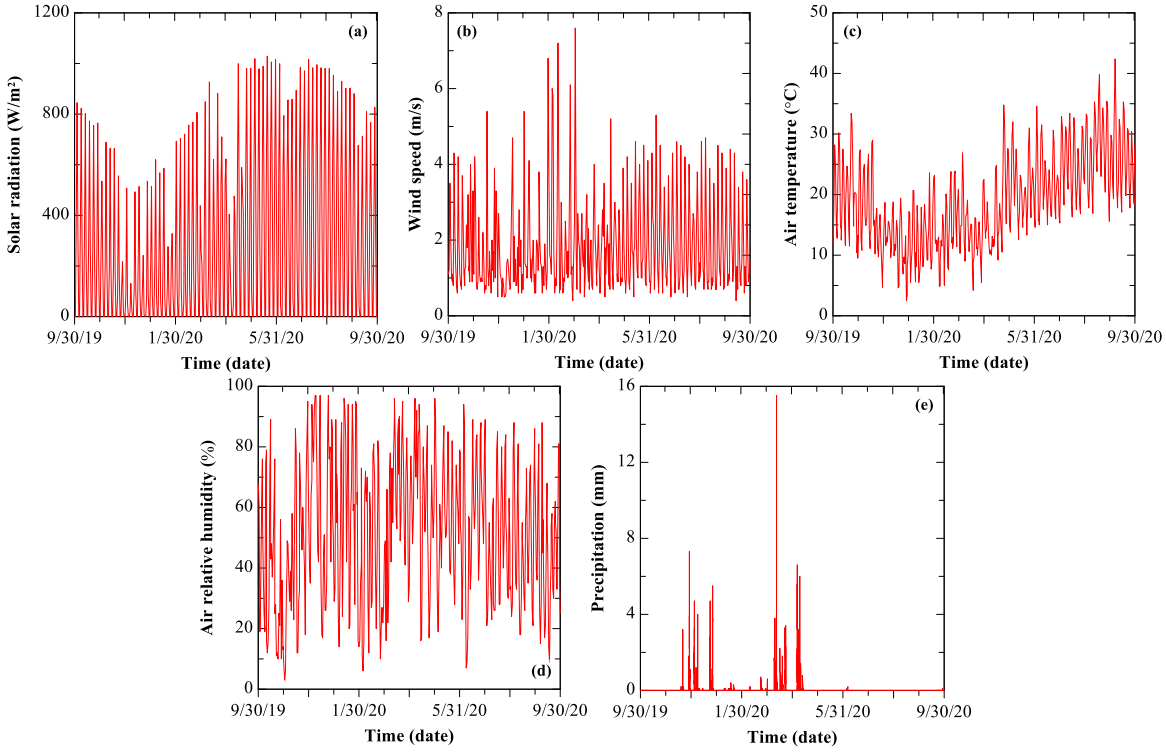

Fig. C2. The meteorological data used to simulate the atmospheric condition for the 2D axisymmetric model: (a) Solar radiation, (b) wind velocity, (c) temperature of the air, (d) relative humidity of the air, and (e) Precipitation

References

[1] S. Assouline, S.W. Tyler, J.S. Selker, I. Lunati, C. Higgins, M. Parlange, Evaporation from a shallow water table: Diurnal dynamics of water and heat at the surface of drying sand, Water Resources Research 49 (7) (2013) 4022–4034.

[2] O. Ozgener, L. Ozgener, J.W. Tester, A practical approach to predict soil temperature variations for geothermal (ground) heat exchangers applications, International Journal of Heat and Mass Transfer 62 (2013) 473–480.

[3] M. Hedayati-Dezfooli, W.H. Leong, An experimental study of coupled heat and moisture transfer in soils at high temperature conditions for a medium coarse soil, International Journal of Heat and Mass Transfer 137 (2019) 372–389.

[4] D.Y. Cherati, O. Ghasemi-Fare, Analyzing transient heat and moisture transport surrounding a heat source in unsaturated porous media using the Green's function, Geothermics 81 (2019) 224–234.

[5] D.Y. Cherati, O. Ghasemi-Fare, Unsaturated thermal consolidation around a heat source, Computers and Geotechnics 134 (2021) 104091.

[6] G. Baroni, A. Facchi, C. Gandolfi, B. Ortuani, D. Horeschi, J. Van Dam, Uncertainty in the determination of soil hydraulic parameters and its influence on the performance of two hydrological models of different complexity, Hydrology and Earth System Sciences 14 (2) (2010) 251–270.

[7] M. Bittelli, F. Ventura, G.S. Campbell, R.L. Snyder, F. Gallegati, P.R. Pisa, Coupling of heat, water vapor, and liquid water fluxes to compute evaporation in bare soils, Journal of Hydrology 362 (3-4) (2008) 191–205.

[8] D. Or, P. Lehmann, E. Shahraeeni, N.J.V.Z.J. Shokri, Advances in soil evaporation physics—A review 12 (4) (2013).

[9] P. Lehmann, S. Assouline, D. Or, Characteristic lengths affecting evaporative drying of porous media, Physical Review E 77 (5) (2008) 056309.

[10] L. Zhang, J. Zhang, L. Zhang, W. Tang, Stability analysis of rainfall-induced slope failure: a review, Proceedings of the Institution of Civil Engineers-Geotechnical Engineering 164 (5) (2011) 299–316.

[11] S. Jasechko, R.G. Taylor, Intensive rainfall recharges tropical groundwaters, Environmental Research Letters 10 (12) (2015) 124015.

[12] J. Vanderborght, T. Fetzer, K. Mosthaf, K.M. Smits, R. Helmig, Heat and water transport in soils and across the soil-atmosphere interface: 1. Theory and different model concepts, Water Resources Research 53 (2) (2017) 1057–1079.

[13] T. Fetzer, J. Vanderborght, K. Mosthaf, K.M. Smits, R. Helmig, Heat and water transport in soils and across the soil-atmosphere interface: 2. Numerical analysis, Water Resources Research 53 (2) (2017) 1080–1100.

[14] W. Wen, Y. Lai, Z. You, Numerical modeling of water–heat–vapor–salt transport in unsaturated soil under evaporation, International Journal of Heat and Mass Transfer 159 (2020) 120114.

[15] T. Bao, S. Liu, Y. Qin, Z. Liu, 3D modeling of coupled soil heat and moisture transport beneath a surface fire, International Journal of Heat and Mass Transfer 149 (2020) 119163.

[16] J. Philip, D. De Vries, Moisture movement in porous materials under temperature gradients, Eos, Transactions American Geophysical Union, 38(2) (1957) 222-232.

[17] J. Benet, P.J.I.J.o.H. Jouanna, M. Transfer, Phenomenological relation of phase change of water in a porous medium: experimental verification and measurement of the phenomenological coefficient, 25(11) (1982) 1747-1754.

[18] J.-C. Benet, A.-L. Lozano, F. Cherblanc, B. Cousin, Phase change of water in a hygroscopic porous medium. Phenomenological relation and experimental analysis for water in soil, Journal of Non-Equilibrium Thermodynamics 34 (2) (2009) 133–153.

[19] K.M. Smits, A. Cihan, T. Sakaki, T.H. Illangasekare, Evaporation from soils under thermal boundary conditions: Experimental and modeling investigation to compare equilibrium-and nonequilibrium-based approaches, Water Resources Research 47 (5) (2011).

[20] Z. Li, J. Vanderborght, K.M. Smits, Evaluation of model concepts to describe water transport in shallow subsurface soil and across the soil–air interface, Transport in porous media 128 (3) (2019) 945–976.

[21] A.C. Trautz, K.M. Smits, A. Cihan, Continuum-scale investigation of evaporation from bare soil under different boundary and initial conditions: An evaluation of nonequilibrium phase change, Water Resources Research 51 (9) (2015) 7630–7648.

[22] A. Moradi, K.M. Smits, N. Lu, J.S. McCartney, Heat transfer in unsaturated soil with application to borehole thermal energy storage, Vadose Zone Journal 15 (10) (2016).

[23] W. Massman, A non-equilibrium model for soil heating and moisture transport during extreme surface heating: the soil (heat-moisture-vapor) HMV-Model Version, Geoscientific Model Development 8 (2015) 3659–3680 8: 3659-3680.

[24] W.J. Massman, The challenges of an in situ validation of a nonequilibrium model of soil heat and moisture dynamics during fires, Hydrology and Earth System Sciences 25 (2) (2021) 685–709.

[25] P. Nuske, V. Joekar-Niasar, R. Helmig, Non-equilibrium in multiphase multicomponent flow in porous media: An evaporation example, International Journal of Heat and Mass Transfer 74 (2014) 128–142.

[26] M.M. Tamizdoust, O. Ghasemi-Fare, Utilization of Nonequilibrium Phase Change Approach to Analyze the Nonisothermal Multiphase Flow in Shallow Subsurface Soils, Water Resources Research 56 (10) (2020) e2020WR027381.

[27] M. Seredyński, M. Wasik, P. Łapka, P. Furmański, Ł. Cieślikiewicz, K. Pietrak, M. Kubiś, T.S. Wiśniewski, M. Jaworski, Analysis of Non-Equilibrium and Equilibrium Models of Heat and Moisture Transfer in a Wet Porous Building Material, Energies 13 (1) (2020) 214.

[28] K.M. Smits, V.V. Ngo, A. Cihan, T. Sakaki, T.H. Illangasekare, An evaluation of models of bare soil evaporation formulated with different land surface boundary conditions and assumptions, Water Resources Research 48 (12) (2012).

[29] K.M. Smits, T. Sakaki, S.E. Howington, J.F. Peters, T.H. Illangasekare, Temperature dependence of thermal properties of sands across a wide range of temperatures (30–70 C), Vadose Zone Journal 12 (1) (2013).

[30] M. Tuller, D. Or, L.M. Dudley, Adsorption and capillary condensation in porous media: Liquid retention and interfacial configurations in angular pores, Water Resources Research 35 (7) (1999) 1949–1964.
[31] A. Revil, N. Lu, Unified water isotherms for clayey porous materials, Water Resources Research 49 (9) (2013) 5685–5699.
[32] M.T. Van Genuchten, A closed-form equation for predicting the hydraulic conductivity of unsaturated soils 1, Soil science society of America journal 44 (5) (1980) 892–898.
[33] Y. Mualem, A new model for predicting the hydraulic conductivity of unsaturated porous media, Water Resources Research 12 (3) (1976) 513–522.
[34] J.G. Hartley, An analysis of the thermal stability of the soil environment of underground electrical cables, Georgia Institute of Technology, 1977.
[35] G. Anders, H. Radhakrishna, Power cable thermal analysis with consideration of heat and moisture transfer in the soil, IEEE Transactions on Power Delivery 3 (4) (1988) 1280–1288.
[36] P. Ocłoń, P. Cisek, M. Pilarczyk, D. Taler, Numerical simulation of heat dissipation processes in underground power cable system situated in thermal backfill and buried in a multilayered soil, Energy Conversion and Management 95 (2015) 352–370.
[37] A. Moradi, K.M. Smits, J. Massey, A. Cihan, J. McCartney, Impact of coupled heat transfer and water flow on soil borehole thermal energy storage (SBTES) systems: Experimental and modeling investigation, Geothermics 57 (2015) 56–72.
[38] T. Başer, Y. Dong, A. Moradi, N. Lu, K. Smits, S. Ge, D. Tartakovsky, J.J.J.o.G. McCartney, G. Engineering, Role of nonequilibrium water vapor diffusion in thermal energy storage systems in the vadose zone, 144(7) (2018) 04018038.
[39] J. Zhang, Q. Chen, C. You, Numerical simulation of mass and heat transfer between biochar and sandy soil, International Journal of Heat and Mass Transfer 91 (2015) 119–126.
[40] M.M. Tamizdoust, O. Ghasemi-Fare, Numerical Analysis on Feasibility of Thermally Induced Pore Fluid Flow in Saturated Soils, in: Eighth International Conference on Case Histories in Geotechnical Engineering, ASCE, Philadelphia, Pennsylvania, 2019, pp. 73–82.
[41] M.M. Tamizdoust, O. Ghasemi-Fare, Comparison of thermo-poroelastic and thermo-poroelastoplastic constitutive models to analyze THM process in clays, in: E3S Web of Conferences, EDP Sciences, 2020, p. 04008.
[42] V.A.F. Costa, Thermodynamic analysis of building heating or cooling using the soil as heat reservoir, International Journal of Heat and Mass Transfer 49 (21) (2006) 4152–4160.
[43] E. Kroener, A. Vallati, M. Bittelli, Numerical simulation of coupled heat, liquid water and water vapor in soils for heat dissipation of underground electrical power cables, Applied Thermal Engineering 70 (1) (2014) 510–523.
[44] M. Hruška, C. Clauser, R.W. De Doncker, The Effect of Drying around Power Cables on the Vadose Zone Temperature, Vadose Zone Journal 17 (1) (2018).
[45] M. Hruška, C. Clauser, R.W. De Doncker, Influence of dry ambient conditions on performance of underground medium-voltage DC cables, Applied Thermal Engineering 149 (2019) 1419–1426.
[46] M.M. Tamizdoust, A. Moradi, O. Ghasemi-Fare, Numerical Analysis of variation of saturation and moisture transport at the vicinity of a heat source, in: Geo-Congress 2020: Geo-Systems, Sustainability, Geoenvironmental Engineering, and Unsaturated Soil Mechanics, American Society of Civil Engineers Reston, VA, 2020, pp. 349–357.
[47] E. Kroener, G.S. Campbell, M. Bittelli, Estimation of thermal instabilities in soils around underground electrical power cables, Vadose Zone Journal 16 (9) (2017) 1–13.
[48] O. Ghasemi-Fare, P. Basu, Influences of ground saturation and thermal boundary condition on energy harvesting using geothermal piles, Energy and Buildings 165 (2018) 340–351.
[49] O. Ghasemi-Fare, P. Basu, A practical heat transfer model for geothermal piles, Energy and Buildings 66 (2013) 470–479.
[50] O. Ghasemi-Fare, P. Basu, Coupling heat and buoyant fluid flow for thermal performance assessment of geothermal piles, Computers and Geotechnics 116 (2019) 103211.
[51] A. Oke, I. Animasaun, W. Mutuku, M. Kimathi, N.A. Shah, S. Saleem, Significance of Coriolis force, volume fraction, and heat source/sink on the dynamics of water conveying 47 nm alumina nanoparticles over a uniform surface, Chinese Journal of Physics 71 (2021) 716–727.
[52] J. Bear, Dynamics of fluids in porous media, Courier Corporation, 2013.
[53] N. Lu, Generalized soil water retention equation for adsorption and capillarity, Journal of Geotechnical and Geoenvironmental Engineering 142 (10) (2016) 04016051.
[54] H.Y. She, B.E. Sleep, The effect of temperature on capillary pressure-saturation relationships for air-water and perchloroethylene-water systems, Water Resources Research 34 (10) (1998) 2587–2597.
[55] S.A. Grant, A. Salehzadeh, Calculation of temperature effects on wetting coefficients of porous solids and their capillary pressure functions, Water Resources Research 32 (2) (1996) 261–270.
[56] I. Animasaun, Effects of thermophoresis, variable viscosity and thermal conductivity on free convective heat and mass transfer of non-darcian MHD dissipative Casson fluid flow with suction and nth order of chemical reaction, Journal of the Nigerian Mathematical Society 34 (1) (2015) 11–31.
[57] S.S. Motsa, I.L. Animasaun, A new numerical investigation of some thermo–physical properties on unsteady MHD non-Darcian flow past an impulsively started vertical surface, Thermal Science 19 (suppl. 1) (2015) 249–258.
[58] T.K. Tokunaga, Hydraulic properties of adsorbed water films in unsaturated porous media, Water resources research 45 (6) (2009).
[59] Z.F. Zhang, Soil water retention and relative permeability for conditions from oven-dry to full saturation, Vadose Zone Journal 10 (4) (2011) 1299–1308.
[60] D. Wang, S. Yates, F. Ernst, Determining soil hydraulic properties using tension infiltrometers, time domain reflectometry, and tensiometers, Soil Science Society of America Journal 62 (2) (1998) 318–325.
[61] J. Niessner, S.M. Hassanizadeh, Non-equilibrium interphase heat and mass transfer during two-phase flow in porous media—theoretical considerations and modeling, Advances in water resources 32 (12) (2009) 1756–1766.
[62] F. Ouedraogo, F. Cherblanc, B. Naon, J.-C. Bénet, Water transfer in soil at low water content. Is the local equilibrium assumption still appropriate? Journal of hydrology 492 (2013) 117–127.
[63] I. Eames, N. Marr, H. Sabir, The evaporation coefficient of water: a review, International Journal of Heat and Mass Transfer 40 (12) (1997) 2963–2973.
[64] R. Marek, J. Straub, Analysis of the evaporation coefficient and the condensation coefficient of water, International Journal of Heat and Mass Transfer 44 (1) (2001) 39–53.
[65] A. Kryukov, V.Y. Levashov, About evaporation–condensation coefficients on the vapor–liquid interface of high thermal conductivity matters, International Journal of Heat and Mass Transfer 54 (13-14) (2011) 3042–3048.
[66] P.C.D. Milly, Moisture and heat transport in hysteretic, inhomogeneous porous media: A matric head-based formulation and a numerical model, Water Resources Research 18 (3) (1982) 489–498.
[67] M.D. Novak, Dynamics of the near-surface evaporation zone and corresponding effects on the surface energy balance of a drying bare soil, Agricultural and Forest Meteorology 150 (10) (2010) 1358–1365.
[68] H. Saito, J. Šimůnek, B.P. Mohanty, Numerical analysis of coupled water, vapor, and heat transport in the vadose zone, Vadose Zone Journal 5 (2) (2006) 784–800.
[69] J. Simunek, M.T. Van Genuchten, M. Sejna, in: The HYDRUS-1D software package for simulating the one-dimensional movement of water, heat, and multiple solutes in variably-saturated media, 3, University of California-Riverside Research Reports, 2005, pp. 1–240.
[70] T.F.M. Chui, D.L. Freyberg, Implementing hydrologic boundary conditions in a multiphysics model, Journal of Hydrologic Engineering 14 (12) (2009) 1374–1377.
[71] B. Choudhury, R. Reginato, S. Idso, An analysis of infrared temperature observations over wheat and calculation of latent heat flux, Agricultural and Forest Meteorology 37 (1) (1986) 75–88.
[72] R. Sviercoski, Y. Efendiev, B. Mohanty, Upscaling the coupled water and heat transport in the shallow subsurface, Water Resources Research 54 (2) (2018) 995–1012.
[73] M. Bittelli, G.S. Campbell, F. Tomei, Soil physics with Python: transport in the soil-plant-atmosphere system, OUP, Oxford, 2015.
[74] M.M. Tamizdoust, O. Ghasemi-Fare, A fully coupled thermo-poro-mechanical finite element analysis to predict the thermal pressurization and thermally induced pore fluid flow in soil media, Computers and Geotechnics 117 (2020) 103250.
[75] B. Mohanty, P. Shouse, M.T. van Genuchten, Spatio-temporal dynamics of water and heat in a field soil, Soil and Tillage Research 47 (1-2) (1998) 133–143.
[76] Y.A. Pachepsky, R. Shcherbakov, G. Varallyay, K. Rajkai, On obtaining soil hydraulic conductivity curves from water retention curves, Pochvovedenie 10 (1984) 60–72.
[77] N. Shokri, P. Lehmann, D. Or, Critical evaluation of enhancement factors for vapor transport through unsaturated porous media, Water resources research 45 (10) (2009).
[78] G. Campbell, J. Jungbauer Jr, W. Bidlake, R. Hungerford, Predicting the effect of temperature on soil thermal conductivity, Soil science 158 (5) (1994) 307–313.